# Uranium isotope evidence for two episodes of deoxygenation during Oceanic Anoxic Event 2

***Author List***

Matthew O. Clarkson[a,1,2], Claudine H. Stirling[a], Hugh C. Jenkyns[b], Alexander J. Dickson[b,c], Don Porcelli[b], Christopher M. Moy[d], Philip A.E. Pogge von Strandmann[e], Ilsa R. Cooke[a] and Timothy M. Lenton[f]

***Published in the Proceedings of the National Academy of Sciences (PNAS), March 5 2018***

***www.pnas.org/cgi/doi/10.1073/pnas.1715278115***

**Affiliations**

[a] *Department of Chemistry, University of Otago, P.O. Box 56, Dunedin 9054, New Zealand*

[b] *Department of Earth Sciences, University of Oxford, South Parks Road, Oxford OX1 3AN, UK*

[c] *Department of Earth Sciences, Royal Holloway University of London, Egham, Surrey, TW20 0EX, UK*

[d] *Department of Geology, University of Otago, P.O. Box 56, Dunedin 9054, New Zealand*

[e] *London Geochemistry and Isotope Centre (LOGIC), Institute of Earth and Planetary Sciences, University College London and Birkbeck, University of London, Gower Street, London WC1E 6BT, UK*

[f] *Earth System Science, College of Life and Environmental Sciences, University of Exeter, Exeter EX4 4QE, UK*

[1]*To whom correspondence should be addressed. Email: matthew.clarkson@erdw.ethz.ch*

[2] *Present address: Institute of Geochemistry and Petrology, Department of Earth Sciences, ETHZ, 8092, Zurich, Switzerland*

***Abstract***

Oceanic Anoxic Event 2 (OAE 2), occurring ~94 million years ago, was one of the most extreme carbon cycle and climatic perturbations of the Phanerozoic Eon. It was typified by a rapid rise in atmospheric $CO_2$, global warming, and marine anoxia, leading to the widespread devastation of marine ecosystems. However, the precise timing and extent to which oceanic anoxic conditions expanded during OAE 2 remains unresolved. We present a new record of global ocean redox changes during OAE 2 using a combined geochemical and carbon cycle modelling approach. We utilize a continuous, high-resolution record of uranium isotopes in pelagic and platform-carbonate sediments to quantify the global extent of seafloor anoxia during OAE 2. This new dataset is then compared to a dynamic model of the coupled global carbon, phosphorus and uranium cycles to test hypotheses for OAE 2 initiation. This unique approach highlights an intra-OAE complexity that has previously been under constrained, characterized by two expansions of anoxia separated by an episode of globally significant reoxygenation coincident with the 'Plenus Cold Event'. Each anoxic expansion event was likely driven by rapid atmospheric $CO_2$ injections from multi-phase Large Igneous Province (LIP) activity.

***Significance Statement***

*Past 'Oceanic Anoxic Events' (OAEs) represent important carbon cycle perturbations that offer the opportunity to study the Earth's response to extreme climate warming. A fundamental limitation for understanding OAEs is quantifying the timing and total extent of ocean anoxia. We present a quantitative account of global redox conditions for OAE 2 (~94 million years ago), using a high-resolution record of uranium isotopes combined with a biogeochemical model. We present new evidence for two discrete intervals of globally extensive anoxia that were coupled to enhanced terrestrial weathering, within the typically defined OAE interval. These anoxic intervals were separated by ocean reoxygenation and the temporary recovery of the carbon cycle.*

***Introduction***

Rapid climatic warming events have repeatedly punctuated Earth's history and have often been associated with prolonged episodes of widespread oceanic anoxia. These intervals represent major disturbances to the global carbon cycle, which contributed to marine faunal turnover and mass extinctions (1). In particular, the Mesozoic Era was characterized by numerous prolonged intervals of globally enhanced anoxia, termed 'Oceanic Anoxic Events' (OAEs) (1). The Mesozoic OAEs are considered the model expression of oceanic anoxia in the Phanerozoic geological record, thus informing studies of past hyperthermal events and future environmental change (2, 3). Despite extensive study, the magnitude and timing of oceanic anoxia for OAEs are still poorly constrained, representing a fundamental limitation for defining these events. We address this shortcoming by presenting a new quantitative record of oceanic anoxia for OAE 2.

OAE 2 is the most widely recognised and severe OAE, occurring at the Cenomanian–Turonian Boundary (~94 Ma) (1) and lasting for up to ~900 thousand years (kyr) (4). A leading hypothesis for the initiation of OAE 2 is through the emplacement of one or more of the Caribbean, Madagascar and High-Arctic Large Igneous Provinces (LIPs) (1, 5-7) and an associated outgassing of $CO_2$ that caused climate warming and accelerated weathering (8). Such processes likely drove an increase in the supply of nutrients, especially phosphorus (P), to the ocean, and thereby increased productivity and oxygen demand through the aerobic degradation of organic matter (1, 5, 9). Productivity was potentially further amplified by the effective recycling of P from sediments overlain by anoxic waters (10-12). Ultimately, this chain of events led to anoxic water-column conditions and the enhanced preservation of organic carbon, which formed distinct black shales in marine sedimentary successions in many ocean basins. The preferential burial of isotopically light carbon (C) also contributed to a broad positive carbon-isotope excursion (CIE) across OAE 2 that is utilized as a global chemo-stratigraphic marker of the event (1). Silicate weathering and organic- carbon burial are vital components of the

global carbon cycle and represent important negative feedback mechanisms that sequester atmospheric $CO_2$ and drive climate stabilization during global warming events (8, 12, 13). However, the detailed behaviour of these recovery processes is currently limited for numerous carbon cycle perturbations in Earth history, including OAEs.

For OAE 2 there is widespread evidence of regionally extensive anoxia and euxinia (anoxic-sulfidic water-column conditions) in disparate localities, leading to benthic faunal extinctions, globally enhanced organic-carbon burial and the sequestration of redox-sensitive and chalcophilic trace metals (1, 9, 12, 14, 15). Oceanic anoxia is, however, a spatially heterogeneous condition, with a highly variable geochemical and sedimentary expression. A dependence on local redox indicators has significantly limited the integration of this important phenomenon into a global carbon cycle framework. To address this limitation, we present a quantitative record of the global extent of anoxia for OAE 2 using new, high-resolution uranium-isotope ($^{238}U/^{235}U$, reformulated as $\delta^{238}U$, see SI) data, in combination with a biogeochemical model that calculates changes in the coupled global C, P and U cycles. These new geochemical data come from well-preserved and extensively studied carbonate sediments that were deposited under oxygenated conditions in the European shelf sea and Tethyan continental margin during OAE 2. The studied sections (Fig. 1) include deeper shelf pelagic foraminiferal-nannofossil carbonates (chalks) from Eastbourne and South Ferriby (United Kingdom), and shallow-water platform carbonates from Raia del Pedale (Italy). We also present additional lithium-isotope data ($^{7}Li/^{6}Li$, reformulated as $\delta^{7}Li$ (8)) for Eastbourne which supplement previously published results (8) to give a more highly resolved complementary record of changes in the global weathering regime during OAE 2.

Under anoxic conditions, oxidized and soluble U(VI) is drawn down from the water column and deposited in sediments as reduced and immobile U(IV), driving seawater U concentrations ([U]) to lower values (16, 17). The primary isotopic fractionation of U is also strongly redox-dependent, whereby $^{238}U$ is preferentially sequestered in anoxic sediments, leaving the residual seawater relatively enriched in $^{235}U$ (18-25). This geochemical behaviour generates lower $\delta^{238}U$ signatures in seawater that can be recorded in contemporary sediments. Moreover, because of the long residence time of U in the modern ocean (320–560 kyrs (16)) sedimentary $\delta^{238}U$ signatures can resolve global changes in oceanic redox conditions (14, 26-29), which cannot be achieved by more traditional proxies.

For OAE 2, application of the U-isotope paleo-redox tracer is limited to a single study of organic-rich black shales ($\delta^{238}U_{shale}$), wherein the data are suggestive of a three-fold increase in the extent of anoxia across the event (14). These data (Fig. 1) are of insufficient temporal resolution to provide insights into the rate and magnitude of ocean redox changes across the event or elucidate the

temporal relationship of ocean anoxia to other aspects of the Earth system response. Furthermore, the fractionation of U into black shales is strongly influenced by local geochemical controls (30) that complicate attempts to infer the 'global' U-isotope signature of oceanic redox changes. By contrast, the U-isotope signature of primary carbonate precipitates ($\delta^{238}U_{carb}$) records the seawater isotopic composition ($\delta^{238}U_{sw}$), with minimal additional fractionation under most environmental conditions (21, 25, 31, 32).

The new datasets presented here are used to test the current hypotheses for OAE 2 initiation, and the resulting biogeochemical changes, by acting as target outputs for the C–P–U model (see Methods and SI). This approach differs from other efforts to model U-isotope data in deep time (14, 26-29), in that it calculates dynamic changes to the wider Earth system, including temperature, weathering, nutrient inputs, anoxia and carbon burial, driven by hypothesized perturbations to the carbon cycle. These changes, in turn, affect the oceanic U cycle. The benefit of this approach is that it gives an internally consistent, quantitative assessment of coupled changes in the carbon cycle.

***Results and Discussion***

***Geochemical Reconstruction of Oceanic Anoxia.*** The stratigraphically expanded Eastbourne section has been extensively studied for a multitude of paleo-environmental proxies owing to its lack of significant diagenetic alteration (1, 8, 15, 33, 34) (see SI). In particular, the carbonates from Eastbourne have very low values of total organic carbon (TOC) (34) and were not subject to appreciable diagenetic sulfate reduction in pore waters (33), which should have minimized alteration of the primary $\delta^{238}U_{carb}$ signatures. As such, the $\delta^{238}U_{carb}$ record for Eastbourne should closely reflect variability in $\delta^{238}U_{sw}$ throughout the OAE 2 interval and is hence used as the primary reference curve in the present study. The $\delta^{238}U_{carb}$ record for Eastbourne has the highest resolution of the three sites and systematic temporal trends are statistically identified using a locally weighted polynomial smoothing function (LOESS) in order to prevent undue emphasis being placed on single data points. The South Ferriby section, although also showing a low degree of diagenetic alteration (see SI), is more lithified than Eastbourne, raising the possibility of greater secondary influences on $\delta^{238}U_{carb}$. It also contains a significant unconformity (Fig. 1) which is overlain by an organic-rich black shale. Mobilization of U from this horizon could potentially explain the comparatively high $\delta^{238}U_{carb}$ values above the unconformity that are more typical of anoxic sediments (18, 19, 23, 30). Deposits at Raia del Pedale show evidence for partial recrystallization and dolomitization of originally mixed aragonite and high-magnesium-calcite producers (see SI). In particular the lowest $\delta^{238}U_{carb}$ of the section are from dolomitized samples with anomalously high U/Ca (Fig. 1 and Fig. S3), consistent with the negative $\delta^{238}U_{carb}$ offset and U enrichment observed in modern dolomites (21, 31).

Multiple lines of evidence support the fidelity of the Eastbourne $\delta^{238}U_{carb}$ record. First, despite potential diagenetic influences in the Raia del Pedale and South Ferriby sections, stability is seen in the $\delta^{238}U_{carb}$ records post-dating OAE 2 at all three sites (Fig. 1). It is important to note that, during this stable post-OAE 2 interval, $\delta^{238}U_{shale}$ values from the organic-rich black shales of Ocean Drilling Program (ODP) site 1261 (14) are ~0.5‰ higher than contemporaneous $\delta^{238}U_{carb}$ (Fig. 1). This offset is consistent with the observed magnitude and direction of U-isotope fractionation during U reduction in modern organic-rich sediments under an anoxic water column (18, 19, 23, 30) and therefore suggests that Eastbourne $\delta^{238}U_{carb}$ closely reflects absolute values in $\delta^{238}U_{sw}$. Furthermore, during this stable period, $\delta^{238}U_{carb}$ from Raia del Pedale and South Ferriby are ~0.2 to 0.3‰ higher than Eastbourne which is consistent with observations from some modern bulk carbonate sediments that show higher $\delta^{238}U_{carb}$ than seawater due to early diagenesis (31). These offsets, compared to Eastbourne, therefore likely reflect the diagenetic gradient between the carbonate sites and support a near-primary $\delta^{238}U_{sw}$ signature at Eastbourne. In addition, there are two systematic decreases in $\delta^{238}U_{carb}$ at Eastbourne (Anoxia Expansion (AE) 1 and AE2, Fig. 2) which are associated with the progressive lowering of U/Ca and other redox-sensitive or chalcophilic trace metals ($TM_{redox}$) at multiple localities, consistent with the removal of these elements into anoxic sediments. Finally, there is a broad coupling between two decreases in the $\delta^{238}U_{carb}$ and $\delta^{7}Li$ records (Fig. 2), which would not be preserved during diagenesis, and substantiates the veracity of both datasets.

At Eastbourne, the onset of the CIE, which typically defines the beginning of OAE 2, is closely associated with a systematic decrease in $\delta^{238}U_{carb}$ from a maximum of -0.24 ± 0.09‰ (2SE) to a minimum of -0.71 ± 0.06‰ (AE1). This drop in values is accompanied by a decrease in $TM_{redox}$ in multiple localities (35-37), including Eastbourne (Fig. 1 & 2) and Raia del Pedale (Fig. 1), suggesting the global expansion of oceanic anoxic conditions. After AE1, $\delta^{238}U_{carb}$ rapidly increases to -0.41 ± 0.07‰ suggesting a decrease in the extent of oceanic anoxia. This dramatic change directly corresponds to the onset of the Plenus Cold Event (PCE), an interval characterized by cooler temperatures at a range of latitudes (35, 38-45). Higher $\delta^{238}U_{carb}$ values averaging -0.38 ± 0.12 ‰ (1sd) were maintained throughout the PCE and correspond to widely observed $TM_{redox}$ enrichments (35-37) (Fig. 1 & 2), indicating the decreased sequestration and oxidative liberation of these metals under more oxygenated conditions (35). The rise in $\delta^{238}U_{carb}$ is also consistent with observations of local benthic faunal re-population and local reoxygenation in some basins, during the PCE (35, 36, 44-47). Importantly, the new $\delta^{238}U_{carb}$ dataset indicates that the PCE reoxygenation was globally significant, returning the ocean to a redox state similar to pre-perturbation conditions.

The end of the PCE corresponds to a second systematic decrease in $\delta^{238}U_{carb}$ (AE2). Again, the concentrations of $TM_{redox}$ decrease at both Eastbourne (Fig. 2) and Raia del Pedale (35) indicating a

return to more expanded oceanic anoxia. Interestingly, the recovery of $\delta^{238}U_{carb}$ from this decrease is poorly defined and appears more gradual, unlike the rapid changes in $\delta^{238}U_{carb}$ observed for the PCE. The lack of a distinct post-OAE 2 recovery may indicate a lingering degree of anoxia after the CIE, or that insufficient time is recorded in these sections to observe the complete re-stabilization of the U and C cycles.

Both AE1 and AE2 are coupled to increased global temperatures, as indicated by $\delta^{18}O$ in Eastbourne (Fig. 2) and organic geochemical proxies in North Atlantic sites (34, 42, 43, 45). Moreover, there is a coupled relationship between decreasing $\delta^{238}U_{carb}$ and $\delta^{7}Li$ during both AE1 and AE2 (Fig. 2), which is suggestive of a shift to a more congruent weathering regime (greater primary mineral dissolution than secondary mineral formation (8, 48) during these two anoxic intervals. These two intervals are also accompanied by independent evidence for an enhanced hydrological cycle (42), together suggesting two discrete periods of enhanced global weathering flux. In contrast to AE1 and AE2, the increasing $\delta^{238}U_{carb}$ and reoxygenation during the PCE corresponds to cooler temperatures and drier conditions (34, 42, 45), as well as the recovery of $\delta^{7}Li$ to more positive values. The coupling of datasets therefore empirically supports the hypothesized link between enhanced weathering activity under warmer climates, increased nutrient fluxes, heightened productivity and expanded oceanic anoxia (1, 8, 9, 42). Furthermore, the first interval of decreasing $\delta^{7}Li$ and $\delta^{238}U_{carb}$ (AE1) also temporally corresponds with a prominent decrease in osmium (Os) isotopes to more unradiogenic, basalt-like signatures that marks the main phase of LIP emplacement associated with the CIE (5-8). The return to more radiogenic Os-isotope signatures is not seen until after the PCE (5-7), reflecting a degree of continued volcanism across the cooling event, although two separate peaks in sedimentary Os concentrations may indicate multiple phases of heightened volcanic activity (5). LIP activity is therefore likely to have driven the two intervals of enhanced weathering activity and resulted in expanded oceanic anoxia.

**A biogeochemical model for OAE 2.** We use a C–P–U model (see SI) to examine if plausible fluxes of $CO_2$ from LIP activity can indeed drive the magnitude of changes observed in $\delta^{238}U_{carb}$, U/Ca and $\delta^{13}C$ at Eastbourne. The model is informed by previously established biogeochemical models (11, 13, 49-52) and calculates the coupled dynamics of C, P and U cycling associated with changes in temperature, weathering and oceanic anoxia, in response to hypothesized $CO_2$ perturbations. The C, P and U cycles are coupled together with the following processes (Fig. S2): (i) LIP $CO_2$ emission, which acts as a source of C; (ii) seafloor spreading, which acts a source of C and a sink of U; (iii) silicate weathering, which is a sink of C and a source of P and U; (iv) primary production of organic matter, which is controlled by P availability and whose burial is a sink of C; (v) oxygen demand in the ocean, which is controlled by primary productivity and organic-matter remineralization rates, and determines

the extent of seafloor anoxia and the burial of U(IV) in anoxic sinks. The burial of organic C also results in an input of $O_2$ to the atmosphere. The U-isotope mass-balance is included in the model, allowing calculated $\delta^{238}U_{sw}$ to trace the predicted extent of seafloor anoxia, whilst accounting for changes in U inputs linked to silicate weathering. Similarly, $\delta^{13}C$ traces relative changes in the sources and sinks of inorganic and organic C.

The model is set up for mid-Cretaceous boundary conditions and the sensitivity to uncertainty in these parameters is discussed in the SI. Background atmospheric $O_2$ is a particularly important boundary condition. Varying $O_2$ in the model serves as a convenient way to account for uncertainty in the pre-existing degree of anoxia during the pre-OAE 2 interval, and hence the size of the ocean U reservoir (Fig. 3) and the sensitivity of the U cycle to $CO_2$ perturbations. Estimates of mid-Cretaceous atmospheric $O_2$ suggest greater than modern levels (49, 51, 53). Here, three baseline settings ($O_2$ = 1.0, 1.1 and 1.2 times present atmospheric levels; PAL) are used to provide an envelope of uncertainty that reasonably captures pre-OAE 2 conditions, satisfies U cycle constraints, and covers the range of uncertainty in $\delta^{238}U_{carb}$ (Fig. 2). The highest $O_2$ concentration setting (1.2 PAL) is the least sensitive to $CO_2$ perturbations and predicts modern levels of pre-OAE seafloor anoxia (0.3%) with the largest oceanic U reservoir (120% of today's size (16), and a higher baseline $\delta^{238}U_{sw}$ of -0.30‰ (compared to modern seawater of -0.39 ± 0.01‰ (18, 21, 25, 30, 54).

**AE1.** Two $CO_2$ emission pulses were modelled, corresponding to AE1 and AE2, where the rate of $CO_2$ injection was kept constant for two discrete intervals of 150 kyrs. According to the C–P–U model, the $\delta^{238}U_{carb}$ excursion during AE1 can be explained by a $CO_2$ degassing event of 0.9–2.25 x $10^{18}$ mol C (i.e. 0.6–1.5 × $10^{13}$ mol C $yr^{-1}$), which represents ~7 to 19% of current total degassing estimates for the combined Caribbean and Madagascar LIPs (see SI). This perturbation results in an increase of atmospheric $CO_2$ to 3.4–4.8 PAL (Fig. 3) and warming of 1.1–2.3°C, similar to independent proxy reconstructions (39, 41, 45). The resultant increase in silicate weathering drives a ~16–39% increase in P input ($F_{Pw}$; Fig. S4), thereby increasing seawater P concentrations ([P]), promoting the expansion of anoxia and the sequestration of reduced U(IV), and preferentially $^{238}U$, in anoxic sediments. The response of ocean nutrient levels, anoxia, and $\delta^{238}U_{sw}$ are delayed compared to the $CO_2$ emission, with the maximum extent of seafloor anoxia occurring up to ~100 kyr after the end of the $CO_2$ injection, and covering between 8 and 15% of the total seafloor area (Fig. 3 and S4). This temporal lag is a function of the positive P feedback mechanism (see Fig. S4). When overlain by anoxic waters, sedimentary P burial efficiency is decreased (10, 11, 50, 51) due to i) the decreased flux of P absorbed to Fe-oxides ($F_{FeP}$) and ii) an increased C/P of buried organic matter ($(C/P)_{organic}$), which supresses productivity-driven increases in the burial of organic bound P ($F_{OrgP}$). These processes inhibit seawater

P depletion in the model and fuel further productivity even when external nutrient inputs are declining, a result which is consistent with published sedimentary P data for OAE 2 (12).

**PCE.** Carbon sequestration from silicate weathering and the burial of marine-derived organic matter increase during AE1 by 16–30% and 20–33% respectively, compared with pre-OAE 2 conditions (Fig. S4). These processes drive the decrease of atmospheric $CO_2$ after the LIP emission ended, resulting in a temperature and weathering decrease, and hence also a decrease in $F_{Pw}$ (Fig. S4). The combination of decreased $F_{Pw}$, continued high Ca-bound P burial ($F_{CaP}$) and high $F_{OrgP}$ burial, leads to a [P] decrease (Fig. S4), and hence biological productivity also decreases. The burial of organic matter under anoxic conditions further drives a minor (~0.02 PAL) net increase in atmospheric $O_2$ during AE1 (Fig. S4). As a result of these controls, ocean oxygenation progresses and is positively re-enforced by the enhanced P removal from increased $F_{FeP}$ burial and decreased $(C/P)_{organic}$ (Fig. S4). In response, $\delta^{238}U_{sw}$ recovers relatively quickly as oceanic anoxia declines, due to the depleted global U reservoir, whilst [U] recovers more slowly, reaching maximum values up to 100 kyrs later (Fig. 3). This process could explain the stratigraphic lag between increasing $\delta^{238}U_{carb}$ and U/Ca during the PCE (Fig. 1 and 2; see the below discussion). During the onset of oxygenation and increase in $\delta^{238}U_{sw}$, $\delta^{13}C$ also continues to rise owing to the slower dynamics of the larger C reservoir, again consistent with the trends shown at Eastbourne for the start of the PCE (Fig. 2). Eventually, the decreased burial of organic matter, and thus isotopically light carbon, during the reoxygenation episode begins to generate the carbon-isotope 'trough' that is used for the chemo-stratigraphic correlation of the PCE (35, 45, 55, 56).

Despite the $\delta^{238}U_{carb}$ increase during the PCE being consistent with the observations of cooler conditions and local benthic reoxygenation (35, 36, 44-47, 57), the magnitude and abrupt rise of the $\delta^{238}U_{carb}$ at Eastbourne is difficult to simulate with the C–P–U model, assuming that this feature is not an artifact of a condensed sedimentary interval. Indeed, the modelled $\delta^{238}U_{sw}$ recovery better corresponds to the later phase of the PCE, when $TM_{redox}$ also recover. The rapidity of the $\delta^{238}U_{carb}$ increase, and delay of the $TM_{redox}$ enrichments, implies a greater sensitivity of $\delta^{238}U_{carb}$ to changing redox conditions, compared to trace-metal concentrations. Such sensitivity was likely driven by an additional decrease in the dynamic residence time of U, already greatly reduced to a minimum of ~45 kyrs ($O_2$ = 1 scenario) during AE1, due to the burial of U(IV) in anoxic sinks. This reduction might have been accomplished by further U drawdown in the 'hypoxic' U sink (i.e. sediments that are reducing at depth, beneath a fully, or poorly oxygenated water column (19)), which is not accounted for in the model, and would have had little impact on $\delta^{238}U_{carb}$. Under such conditions $\delta^{238}U_{carb}$ would more precisely capture the onset of reoxygenation than $TM_{redox}$. Alternatively, this model–data discrepancy may be explained by the oxidation and loss of U from shales previously deposited under anoxic conditions, as has been observed in modern continental-margin sediments (58), and is similar to the

mechanism proposed to explain transiently light $\delta^{34}S_{CAS}$ values during the PCE (15, 35). This additional supply of isotopically heavy U to the ocean would act to amplify the $\delta^{238}U_{sw}$ increase due to the decrease in anoxic sinks, and could further explain the faster response compared to $TM_{redox}$. It is also plausible that reoxygenation could have been accelerated by mechanisms not considered in our model, such as sea level or temperature changes (9, 59), or the additional supply of $O_2$ caused by pyrite burial (49, 53).

**AE2.** An assumed second $CO_2$ injection, of lesser magnitude (0.4–1.05 x $10^{13}$ molC $yr^{-1}$) but of the same duration as the first event, generates a return to warmer conditions after the PCE. This increase in temperature results in a return of widespread anoxia and a smaller negative shift in $\delta^{238}U_{sw}$ by -0.2‰, equivalent to an expansion of oceanic anoxia of 3–8% of the total seafloor area. This modelled $CO_2$ injection also results in the addition of isotopically light carbon to the ocean-atmosphere system that augments the decrease in $^{12}C$-enriched carbon burial during the PCE reoxygenation episode, thereby accelerating the development of the $\delta^{13}C$ 'trough' of the PCE. Despite this minor negative excursion, relatively elevated $\delta^{13}C$ values occur throughout the entire OAE 2 interval owing to the slower dynamics of the relatively large carbon reservoir.

**Wider Implications for OAEs.** Characterizing the timing, duration and extent of oceanic anoxia during OAE 2 is fundamental to understanding the driving mechanisms of these extreme perturbations to the carbon cycle and climate system. In an attempt to replicate the distribution of anoxia indicated by local redox proxies, Earth System modelling suggests 50% of the global ocean volume was dysoxic or anoxic (9) whilst the shale-derived $\delta^{238}U$ estimate suggests only 1–2% of the seafloor was overlain by anoxic waters (14). By contrast, the new carbonate-derived $\delta^{238}U$ dataset presented here provides a better systematic resolution of the timing and magnitude of ocean deoxygenation (Fig. 1), suggesting that between 8% and 15% of the seafloor was overlain by an anoxic water column. This reconstruction is in close agreement with recent estimates from thallium isotopes (60) and is compatible with 2–5% of seafloor being euxinic, based on modelling of the sulfur- and molybdenum-isotope systems (15, 46, 61), as this extreme chemical state would only make up a fraction of the total anoxic ocean, and $\delta^{238}U$ does not discriminate between anoxic and euxinic redox states. The importance of differentiating these two redox states is increasingly being recognized for periods of expanded anoxia (e.g. 62). Crucially, the high resolution of the $\delta^{238}U_{carb}$ data uniquely resolves at least two fluctuations between episodes of globally expanded and contracted anoxia during the traditionally defined OAE 2 interval. Such findings are likely applicable for other OAEs where there are suggestions of local redox and temperature variability, such as the Aptian OAE 1a (1).

The C–P–U model successfully generates the magnitude of U-isotope excursions through fairly conservative $CO_2$ degassing levels and subsequent changes in global temperature. These amounts of

$CO_2$ degassing probably represent upper estimates since the model does not consider many contributory deoxygenation mechanisms, including the inverse relationship between temperature and $O_2$ solubility, or changes in $O_2$ supply through variable ocean ventilation rates (9). We suggest that these additional mechanisms are of second-order importance to changes in terrestrial weathering for driving OAE 2, although they could help refine our understanding of the precise temporal and geographical distribution of oceanic redox changes.

In summary, the coupled geochemical and modelling approach adopted here for OAE 2 allows for an internally consistent examination of global-scale deoxygenation during carbon cycle perturbation events. The new U-isotope dataset highlights globally significant oscillations in oceanic redox conditions within the traditionally defined OAE 2 interval that are closely coupled to changes in global temperature and hydrological regime. The C–P–U model successfully reproduces the trends in $\delta^{238}U_{carb}$ through discrete atmospheric $CO_2$ injections, suggesting that the exceptional longevity of OAE 2 was the result of multi-phase LIP activity.

## Materials and Methods

***Uranium-isotope analysis.*** Carbonate samples were mechanically cleaned for weathered surfaces. Sample powders underwent oxidative-reductive cleaning (63, 64), before selective digestion using 1 M buffered sodium acetate. U-isotope composition was determined using a $^{236}U$-$^{233}U$ double spike to correct for instrumental mass fractionation, where uranium was pre-concentrated by co-precipitation and purified by ion-exchange chromatographic procedures using a single column packed with UTEVA resin (Eichrom Technologies, USA) (20, 21, 23, 65, 66). Uranium-isotope measurements were performed by multiple-collector inductively coupled plasma mass spectrometer (MC-ICP-MS) at the Centre for Trace Element Analysis, University of Otago, New Zealand (19, 21-23). **Lithium-isotope methods.** An additional 8 samples were analyzed from the Eastbourne section for Li isotopes, to increase the resolution of the already existing dataset, following the same original protocols (8). Carbonate samples were leached using 0.1 M HCl for 1 hr and sample solutions were purified using a two-stage cation-exchange procedure. Analyses were performed by MC-ICP-MS at Oxford University, U.K. (8). **Coupled C–P–U model.** The box-model is a simplified version of elements of the Geochemical Carbon cycle model (GEOCARB) and the Carbon, Oxygen, Phosphorus, Sulphur and Evolution (COPSE) Earth System model (11, 13, 49-52), focusing exclusively on the shorter term processes of the carbon and phosphorus cycles. The model incorporates U reservoirs and the isotopic mass-balance equations for C and U isotopes as tracers of the predicted outcomes to assumed $CO_2$ emission perturbations.

## Acknowledgments

We thank the anonymous reviewers of this work for their constructive inputs. We thank Malcolm Reid and David Barr for laboratory support. For their contributions to this work MOC, CHS, CMM, IRC and HCJ were supported by the Marsden Fund Council from government funding, managed by the Royal Society of New Zealand (UOO1314). T.M.L. was supported by the Natural Environment Research Council "Jurassic Earth System and Timescale" large grant and a Royal Society Wolfson Research Merit Award. P.A.E.P.v.S. was funded by European Research Council Consolidator Grant 682760 CONTROLPASTCO2.

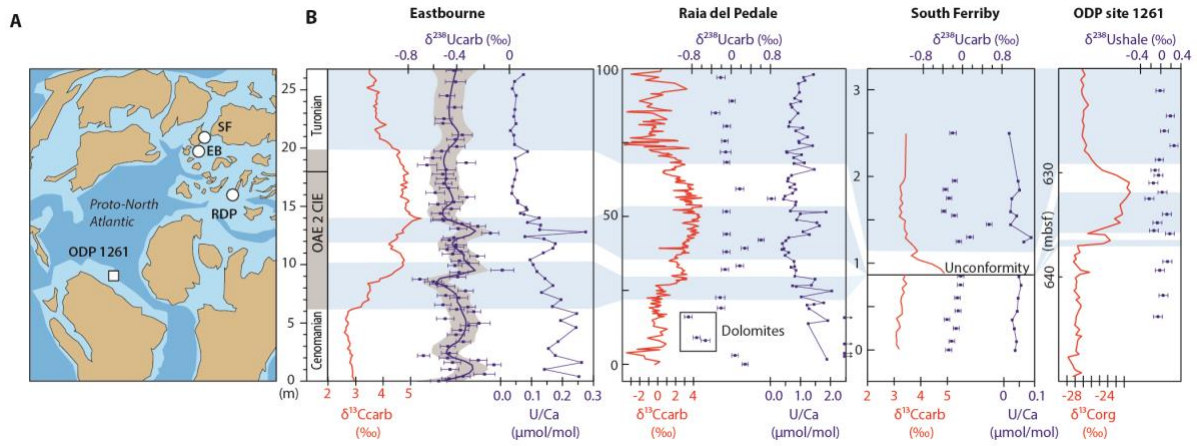


**Fig. 1: A**. Paleogeographic reconstruction showing locations of Eastbourne (EB), Raia del Pedale (RDP), South Ferriby (SF) and ODP site 1261, modified with permission from (67) **B.** $\delta^{13}C$ (15, 34, 68), $\delta^{238}U_{carb}$ (±2SE) and U/Ca (35 and this study) for EB, RDP and SF in comparison to $\delta^{13}C_{org}$ and $\delta^{238}U$ from black shales at ODP site 1261 (14, 55). Correlations (blue shading) are from previous work (8, 15, 35).

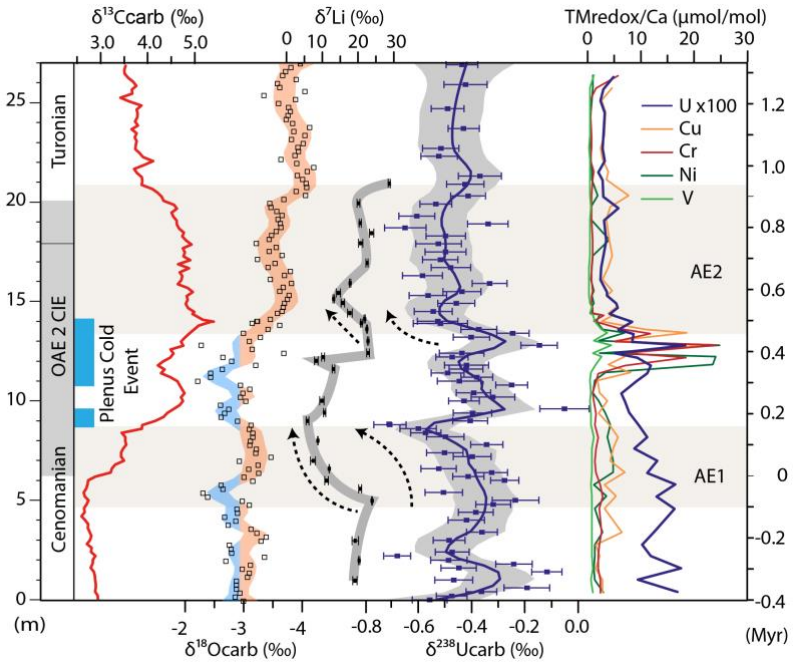


**Fig. 2:** Complementary geochemical datasets ($\delta^{13}C$, $\delta^{18}O$ and $\delta^{7}Li$) (8, 34), together with the $\delta^{238}U_{carb}$ and $TM_{redox}$ datasets for Eastbourne (35). 'Anoxic Expansion' episodes (AE1 and AE2) are identified from coupled negative $\delta^{238}U_{carb}$ excursions and $TM_{redox}$ decreases. Unusual boreal faunas (blue bar) and less negative $\delta^{18}O$ are indicative of cooler waters and mark the 'Plenus Cold Event' (PCE) (35, 38, 56). Black dashed arrows indicate periods of broad coupling between $\delta^{7}Li$ and $\delta^{238}U_{carb}$. The positive $\delta^{13}C$ excursion (34) is traditionally used to define OAE 2 (grey shading). Timescale (right axis) is based on estimates for OAE 2 of up to ~900 kyrs (4) and a linear age model, with 0 kyrs marking the start of the CIE.

374

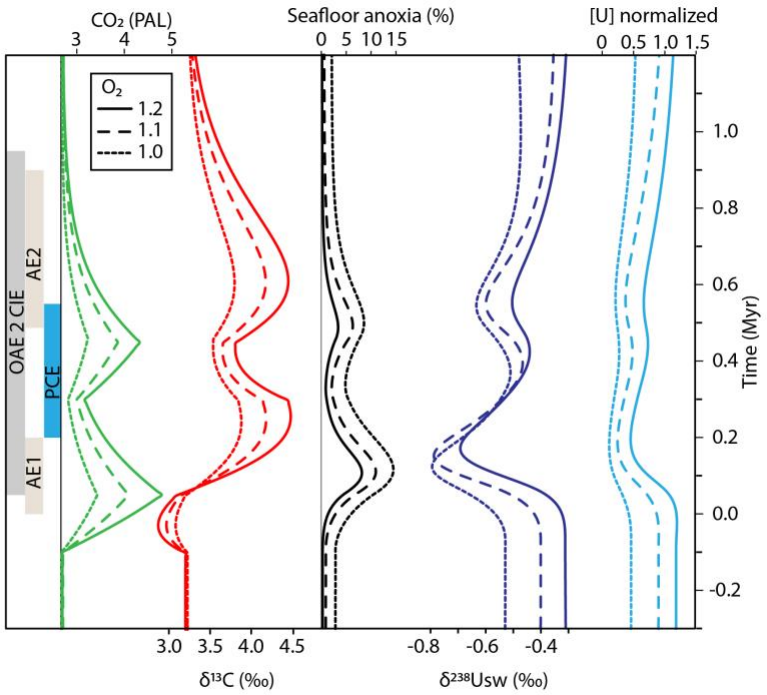


375

376

377 **Fig 3:** C–P–U model outputs in relation to events of OAE 2 identified in the $\delta^{238}U_{carb}$ dataset of this

378 study (upper panel). Time (vertical axis) is given relative to the approximate start of the CIE, as in Fig.

379 2.

380

**References**


1. Jenkyns HC (2010) Geochemistry of oceanic anoxic events. *Geochemistry Geophysics Geosystems.* 11 Q03004, doi:10.1029/2009gc002788.
2. Watson AJ, Lenton TM, & Mills BJW (2017) Ocean deoxygenation, the global phosphorus cycle and the possibility of human-caused large-scale ocean anoxia. *Philosophical Transactions of the Royal Society A: Mathematical, Physical and Engineering Sciences* 375A.
3. Dickson AJ*, et al.* (2014) The spread of marine anoxia on the northern Tethys margin during the Paleocene‐Eocene Thermal Maximum. *Paleoceanography* 29(6):471-488.
4. Eldrett JS*, et al.* (2015) An astronomically calibrated stratigraphy of the Cenomanian, Turonian and earliest Coniacian from the Cretaceous Western Interior Seaway, USA: Implications for global chronostratigraphy. *Cretaceous Research* 56:316–344.
5. Turgeon SC & Creaser RA (2008) Cretaceous Oceanic Anoxic Event 2 triggered by a massive magmatic episode. *Nature* 454(7202):323–326.
6. Du Vivier AD*, et al.* (2014) Marine $^{187}Os/^{188}Os$ isotope stratigraphy reveals the interaction of volcanism and ocean circulation during Oceanic Anoxic Event 2. *Earth and Planetary Science Letters* 389:23–33.
7. Du Vivier A, Selby D, Condon D, Takashima R, & Nishi H (2015) Pacific $^{187}Os/^{188}Os$ isotope chemistry and U–Pb geochronology: Synchroneity of global Os isotope change across OAE 2. *Earth and Planetary Science Letters* 428:204-216.
8. Pogge von Strandmann PAE, Jenkyns HC, & Woodfine RG (2013) Lithium isotope evidence for enhanced weathering during Oceanic Anoxic Event 2. *Nat. Geosci.* 6(8):668–672.
9. Monteiro F, Pancost R, Ridgwell A, & Donnadieu Y (2012) Nutrients as the dominant control on the spread of anoxia and euxinia across the Cenomanian‐Turonian oceanic anoxic event (OAE 2): Model‐data comparison. *Paleoceanography.* 27:(4).PA4209, doi:10.1029/2012PA002351.
10. Van Cappellen P & Ingall ED (1994) Benthic phosphorus regeneration, net primary production, and ocean anoxia - a model of the coupled marine biogeochemical cycles of carbon and phosphorus. *Paleoceanography* 9(5):677-692.
11. Handoh IC & Lenton TM (2003) Periodic mid-Cretaceous Oceanic Anoxic Events linked by oscillations of the phosphorus and oxygen biogeochemical cycles. *Global Biogeochemical Cycles* 17(4).
12. Mort HP*, et al.* (2007) Phosphorus and the roles of productivity and nutrient recycling during Oceanic Anoxic Event 2. *Geology* 35(6):483–486.

13. Berner RA & Kothavala Z (2001) GEOCARB III: A revised model of atmospheric $CO_2$ over Phanerozoic time. *American Journal of Science* 301(2):182–204.
14. Montoya-Pino C*, et al.* (2010) Global enhancement of ocean anoxia during Oceanic Anoxic Event 2: A quantitative approach using U isotopes. *Geology* 38(4):315–318.
15. Owens JD*, et al.* (2013) Sulfur isotopes track the global extent and dynamics of euxinia during Cretaceous Oceanic Anoxic Event 2. *Proceedings of the National Academy of Sciences of the United States of America* 110(46):18407–18412.
16. Dunk R, Mills R, & Jenkins W (2002) A reevaluation of the oceanic uranium budget for the Holocene. *Chem. Geol.* 190(1):45–67.
17. Anderson R (1987) Redox behavior of uranium in an anoxic marine basin. *Uranium* 3(2-4):145–164.
18. Andersen MB*, et al.* (2016) Closing in on the marine $^{238}U/^{235}U$ budget. *Chem. Geol.* 420:11–22.
19. Andersen MB, Stirling CH, & Weyer S (2017) Uranium isotope fractionation. *Rev. Mineral. Geochem* 82(1):799–850.
20. Stirling CH, Andersen MB, Warthmann R, & Halliday AN (2015) Isotope fractionation of $^{238}U$ and $^{235}U$ during biologically-mediated uranium reduction. *Geochimica et Cosmochimica Acta* 163:200–218.
21. Stirling CH, Andersen MB, Potter E-K, & Halliday AN (2007) Low-temperature isotopic fractionation of uranium. *Earth and Planetary Science Letters* 264(1):208–225.
22. Hinojosa JL, Stirling CH, Reid MR, Moy CM, & Wilson GS (2016) Trace metal cycling and $^{238}U/^{235}U$ in New Zealand's fjords: Implications for reconstructing global paleoredox conditions in organic-rich sediments. *Geochimica et Cosmochimica Acta* 179:89–109.
23. Rolison JM, C.H.Stirling, Middag R, & Rijkenberg MJA (2017) Uranium stable isotope fractionation in the Black Sea: Modern calibration of the $^{238}U/^{235}U$ paleoredox proxy. . *Geochimica et Cosmochimica Acta* 203:69–88.
24. Noordmann J*, et al.* (2015) Uranium and molybdenum isotope systematics in modern euxinic basins: Case studies from the central Baltic Sea and the Kyllaren fjord (Norway). *Chem. Geol.* 396:182–195.
25. Weyer S*, et al.* (2008) Natural fractionation of $^{238}U/^{235}U$. *Geochimica et Cosmochimica Acta* 72(2):345-359.
26. Brennecka GA, Herrmann AD, Algeo TJ, & Anbar AD (2011) Rapid expansion of oceanic anoxia immediately before the end-Permian mass extinction. *Proceedings of the National Academy of Sciences of the United States of America* 108(43):17631–17634.

27. Dahl TW*, et al.* (2014) Uranium isotopes distinguish two geochemically distinct stages during the later Cambrian SPICE event. *Earth and planetary science letters* 401:313–326.
28. Lau KV*, et al.* (2016) Marine anoxia and delayed Earth system recovery after the end-Permian extinction. *Proceedings of the National Academy of Sciences* 113(9):2360–2365.
29. Elrick M*, et al.* (2017) Global-ocean redox variation during the middle-late Permian through Early Triassic based on uranium isotope and Th/U trends of marine carbonates. *Geology* 45(2):163-166.
30. Andersen M*, et al.* (2014) A modern framework for the interpretation of $^{238}U/^{235}U$ in studies of ancient ocean redox. *Earth and Planetary Science Letters* 400:184–194.
31. Romaniello SJ, Herrmann AD, & Anbar AD (2013) Uranium concentrations and $^{238}U/^{235}U$ isotope ratios in modern carbonates from the Bahamas: Assessing a novel paleoredox proxy. *Chem. Geol.* 362:305–316.
32. Chen X, Romaniello SJ, Herrmann AD, Wasylenki LE, & Anbar AD (2016) Uranium isotope fractionation during coprecipitation with aragonite and calcite. *Geochimica et Cosmochimica Acta* 188:189–207.
33. Owens JD*, et al.* (2012) Iron isotope and trace metal records of iron cycling in the proto‐North Atlantic during the Cenomanian‐Turonian oceanic anoxic event (OAE 2). *Paleoceanography.* 27.PA3223, doi:10.1029/2012PA002328.
34. Tsikos H*, et al.* (2004) Carbon-isotope stratigraphy recorded by the Cenomanian–Turonian Oceanic Anoxic Event: correlation and implications based on three key localities. *J. Geol. Soc.* 161(4):711–719.
35. Jenkyns HC, Dickson AJ, Ruhl M, & Van den Boorn SHJM (2017) Basalt–seawater interaction, the Plenus Cold Event, enhanced weathering, and geochemical change: deconstructing OAE 2 (Cenomanian–Turonian, Late Cretaceous). *Sedimentology* 64:16–43.
36. Eldrett JS, Minisini D, & Bergman SC (2014) Decoupling of the carbon cycle during Ocean Anoxic Event 2. *Geology* 42(7):567–570.
37. Snow LJ, Duncan RA, & Bralower TJ (2005) Trace element abundances in the Rock Canyon Anticline, Pueblo, Colorado, marine sedimentary section and their relationship to Caribbean plateau construction and Ocean Anoxic Event 2. *Paleoceanography.* 20.doi:10.1029/2004PA001093.
38. Gale AS & Christensen WK (1996) Occurrence of the belemnite *Actinocamax plenus* in the Cenomanian of SE France and its significance. *Bulletin of the Geological Society of Denmark* 43:68–77.

39. Voigt S, Gale AS, & Flögel S (2004) Midlatitude shelf seas in the Cenomanian–Turonian greenhouse world: Temperature evolution and North Atlantic circulation. *Paleoceanography.* 19.PA4020, doi:10.1029/2004PA001015.
40. Voigt S, Gale AS, & Voigt T (2006) Sea-level change, carbon cycling and palaeoclimate during the Late Cenomanian of northwest Europe; an integrated palaeoenvironmental analysis. *Cretaceous Research* 27(6):836-858.
41. Voigt S, Wilmsen M, Mortimore R, & Voigt T (2003) Cenomanian palaeotemperatures derived from the oxygen isotopic composition of brachiopods and belemnites: evaluation of Cretaceous palaeotemperature proxies. *International Journal of Earth Sciences* 92(2):285-299.
42. van Helmond NA*, et al.* (2014) A perturbed hydrological cycle during Oceanic Anoxic Event 2. *Geology* 42(2):123-126.
43. Sinninghe Damsté JS, van Bentum EC, Reichart G-J, Pross J, & Schouten S (2010) A $CO_2$ decrease-driven cooling and increased latitudinal temperature gradient during the mid-Cretaceous Oceanic Anoxic Event 2. *Earth and Planetary Science Letters* 293(1):97–103.
44. Jarvis I, Lignum JS, Gröcke DR, Jenkyns HC, & Pearce MA (2011) Black shale deposition, atmospheric $CO_2$ drawdown, and cooling during the Cenomanian–Turonian Oceanic Anoxic Event. *Paleoceanography.* 26:(3).PA3201, doi:10.1029/2010PA002081.
45. Forster A, Schouten S, Moriya K, Wilson PA, & Sinninghe Damsté JS (2007) Tropical warming and intermittent cooling during the Cenomanian/Turonian Oceanic Anoxic Event 2: Sea surface temperature records from the equatorial Atlantic. *Paleoceanography.* 22.PA1219, doi:10.1029/2006PA001349.
46. Dickson AJ, Jenkyns HC, Porcelli D, van den Boorn S, & Idiz E (2016) Basin-scale controls on the molybdenum-isotope composition of seawater during Oceanic Anoxic Event 2 (Late Cretaceous). *Geochimica et Cosmochimica Acta* 178:291–306.
47. Kuhnt W, Luderer F, Nederbragt S, Thurow J, & Wagner T (2005) Orbital-scale record of the late Cenomanian–Turonian oceanic anoxic event (OAE 2) in the Tarfaya Basin (Morocco). *International Journal of Earth Sciences* 94(1):147–159.
48. Pogge von Strandmann PAE & Henderson GM (2015) The Li isotope response to mountain uplift. *Geology* 43(1):67–70.
49. Bergman JM, Lenton TM, & Watson AJ (2004) COPSE: A new model of biogeochemical cycling over Phanerozoic time. *American Journal of Science* 304(397).
50. Lenton TM & Watson AJ (2000) Redfield revisited: 1. Regulation of nitrate, phosphate, and oxygen in the ocean. *Global Biogeochemical Cycles* 14(1):225–248.

51. Lenton TM & Watson AJ (2000) Redfield revisited: 2. What regulates the oxygen content of the atmosphere? *Global Biogeochemical Cycles* 14(1):249–268.
52. Slomp CP & Van Cappellen P (2007) The global marine phosphorus cycle: sensitivity to oceanic circulation. *Biogeosciences* 4(2):155–171.
53. Mills BJ, Belcher CM, Lenton TM, & Newton RJ (2016) A modeling case for high atmospheric oxygen concentrations during the Mesozoic and Cenozoic. *Geology* 44(12):1023–1026.
54. Tissot FL & Dauphas N (2015) Uranium isotopic compositions of the crust and ocean: age corrections, U budget and global extent of modern anoxia. *Geochimica et Cosmochimica Acta* 167:113–143.
55. Erbacher J, Friedrich O, Wilson PA, Birch H, & Mutterlose J (2005) Stable organic carbon isotope stratigraphy across Oceanic Anoxic Event 2 of Demerara Rise, western tropical Atlantic. *Geochemistry, Geophysics, Geosystems.* 6.doi:10.1029/2004GC000850.
56. Gale A, Jenkyns H, Kennedy W, & Corfield R (1993) Chemostratigraphy versus biostratigraphy: data from around the Cenomanian–Turonian boundary. *J. Geol. Soc.* 150:29–32.
57. Friedrich O (2010) Benthic foraminifera and their role to decipher paleoenvironment during mid-Cretaceous Oceanic Anoxic Events–the “anoxic benthic foraminifera” paradox. *Revue de micropaléontologie* 53(3):175–192.
58. Morford JL, Martin WR, & Carney CM (2009) Uranium diagenesis in sediments underlying bottom waters with high oxygen content. *Geochimica et Cosmochimica Acta* 73(10):2920–2937.
59. Ozaki K & Tajika E (2013) Biogeochemical effects of atmospheric oxygen concentration, phosphorus weathering, and sea-level stand on oceanic redox chemistry: Implications for greenhouse climates. *Earth and Planetary Science Letters* 373:129–139.
60. Ostrander CM, Owens JD, & Nielsen SG (2017) Constraining the rate of oceanic deoxygenation leading up to a Cretaceous Oceanic Anoxic Event (OAE-2:~ 94 Ma). *Science Advances* 3(8):e1701020.
61. Dickson AJ*, et al.* (2016) Corrigendum to" Basin-scale controls on the molybdenum-isotope composition of seawater during Oceanic Anoxic Event 2 (Late Cretaceous)"[Geochim. Cosmochim. Acta 178 (2016) 291-306]. *Geochimica et Cosmochimica Acta* 189:404–405.
62. Poulton SW & Canfield DE (2011) Ferruginous Conditions: A Dominant Feature of the Ocean through Earth's History. *Elements* 7(2):107-112.
63. Bian N & Martin PA (2010) Investigating the fidelity of Mg/Ca and other elemental data from reductively cleaned planktonic foraminifera. *Paleoceanography* 25.

549 64. Boyle E & Rosenthal Y (1996) Chemical hydrography of the South Atlantic during the last
550 glacial maximum: Cd vs. $\delta^{13}C$. *The South Atlantic*, (Springer), pp 423-443.
551 65. Amelin Y*, et al.* (2010) U–Pb chronology of the Solar System's oldest solids with variable $^{238}U/^{235}U$. *Earth and Planetary Science Letters* 300(3):343–350.
553 66. Murphy MJ, Stirling CH, Kaltenbach A, Turner SP, & Schaefer BF (2014) Fractionation of
554 $^{238}U/^{235}U$ by reduction during low temperature uranium mineralisation processes. *Earth and*
555 *Planetary Science Letters* 388:306–317.
556 67. Zhou X*, et al.* (2015) Upper ocean oxygenation dynamics from I/Ca ratios during the
557 Cenomanian–Turonian OAE 2. *Paleoceanography* 30:510-526.
558 68. Jenkyns HC, Matthews A, Tsikos H, & Erel Y (2007) Nitrate reduction, sulfate reduction, and
559 sedimentary iron isotope evolution during the Cenomanian‐Turonian oceanic anoxic event.
560 *Paleoceanography.* 22.PA3208, doi:10.1029/2006PA001355.
561 69. Andersen MB*, et al.* (2015) The terrestrial uranium isotope cycle. *Nature* 517(7534):356–
562 359.
563 70. Tessier A, Campbell PG, & Bisson M (1979) Sequential extraction procedure for the
564 speciation of particulate trace metals. *Anal. Chem.* 51(7):844–851.
565 71. Canfield DE (1998) A new model for Proterozoic ocean chemistry. *Nature* 396(6710):450–
566 453.
567 72. Lenton TM & Daines SJ (2017) Biogeochemical transformations in the history of the ocean.
568 *Annual Review of Marine Science* 9:31–58.
569 73. Helly JJ & Levin LA (2004) Global distribution of naturally occurring marine hypoxia on
570 continental margins. *Deep Sea Research Part I: Oceanographic Research Papers* 51(9):1159–
571 1168.
572 74. Jones CE & Jenkyns HC (2001) Seawater strontium isotopes, oceanic anoxic events, and
573 seafloor hydrothermal activity in the Jurassic and Cretaceous. *American Journal of Science*
574 301(2):112–149.
575 75. Mills B, Daines SJ, & Lenton TM (2014) Changing tectonic controls on the long‐term carbon
576 cycle from Mesozoic to present. *Geochemistry, Geophysics, Geosystems* 15(12):4866–4884.
577 76. Holmden C, Amini M, & Francois R (2015) Uranium isotope fractionation in Saanich Inlet: A
578 modern analog study of a paleoredox tracer. *Geochimica et Cosmochimica Acta* 153:202–
579 215.
580 77. Noordmann J, Weyer S, Georg RB, Jöns S, & Sharma M (2015) $^{238}U/^{235}U$ isotope ratios of
581 crustal material, rivers and products of hydrothermal alteration: new insights on the oceanic
582 U isotope mass balance. *Isotopes in environmental and health studies*:1–23.

78. Eldhom O & Coffin MF (2000) Large igneous provinces and plate tectonics. *The history and dynamics of global plate motions*, (American Geophysical Union, Geophysical Monograph), Vol 121, pp 309–326.
79. Thordarson T & Self S (1996) Sulfur, chlorine and fluorine degassing and atmospheric loading by the Roza eruption, Columbia River Basalt Group, Washington, USA. *Journal of Volcanology and Geothermal Research* 74(1–2):49–73.
80. McManus J*, et al.* (2006) Molybdenum and uranium geochemistry in continental margin sediments: paleoproxy potential. *Geochimica et Cosmochimica Acta* 70(18):4643–4662.
81. Hood Av*, et al.* (2016) Integrated geochemical-petrographic insights from component-selective $\delta^{238}U$ of Cryogenian marine carbonates. *Geology* 44(11):935–938.
82. Keller G, Han Q, Adatte T, & Burns SJ (2001) Palaeoenvironment of the Cenomanian–Turonian transition at Eastbourne, England. *Cretaceous Research* 22(4):391–422.
83. Wray DS & Gale AS (2006) The palaeoenvironment and stratigraphy of Late Cretaceous Chalks. *Proceedings of the Geologists' Association* 117(2):145-162.

**Supplementary Information**

**SI Materials and Methods**

***Reagents***. All reagents used were of ultra-high purity and prepared in-house by sub-boiling quartz and/or teflon distillation (HF, $HNO_3$, HCl, $CH_3COOH$) or purchased commercially from Thermo Fisher or Sigma Aldrich, NZ.

***Sample Preparation.*** Weathered surfaces were removed from samples under dry conditions using a Dremel microdrill before sonication in high-purity Milli-Q water (>18.2 MΩ cm; Millipore, USA) to remove surface contaminants. Samples were dried in an oven at 40˚C and then powdered in a laminar flow hood (Class 100; ISO 5) using an agate pestle and mortar, which was cleaned between samples using 99.995% $SiO_2$ sand and high-purity ethanol. Powdered samples, comprising 1–2 g, were subject to reductive-oxidative cleaning (63, 64) using 1 M hydrous hydrazine + 0.25 M citric acid in 16 M ammonia solution, followed by 1% $H_2O_2$ in 0.1 M NaOH. Repeated MilliQ rinses were performed between cleaning steps. Such cleaning techniques remove potential contamination from residual organic matter and ferro-manganese coatings and are particularly important for extracting primary U/Ca ratios in foraminifera tests (63) and $\delta^{238}U$ signatures from basalts (69). Cleaned powders were digested using 0.6 M or 1 M sodium acetate solution (buffered to a pH of 5) (70) at room temperature for 48 hrs in order to selectively digest carbonate phases and avoid U contributions from detrital silicates

***Ion Exchange Chemical Preparation of Samples for Uranium-Isotope Analysis.*** Uranium-isotope composition was determined using a $^{236}U$-$^{233}U$ double spike to correct for instrumental mass fractionation by adapting methods reported previously (20, 21, 23, 65, 66). The digest supernates were evaporated to dryness in the presence of excess 7 M $HNO_3$ to prevent the formation of sodium acetate precipitates. The final nitrate precipitates were then dissolved in 1.5 M $HNO_3$. This digest was subsampled, diluted and analyzed via quadrupole ICP-MS using an Agilent 7500 instrument (Agilent Technologies, USA) at the Centre for Trace Element Analysis, University of Otago, New Zealand to determine the approximate U concentration in order to inform the double-spike addition calculation. Based on this U concentration, samples were again subsampled into PFA vials to achieve a total uranium mass of 30 to 150 ng and double spiked to give a $^{236}U/^{235}U$ ratio of approximately 3. Solutions were refluxed for 24 hrs to ensure complete spike-sample equilibration. Due to the high matrix content of the carbonate digests, co-precipitation using pre-cleaned $FeCl_3$ and ammonia solution was conducted to remove the majority of Na and Ca from the sample and prevent overwhelming the ion-

exchange resin with matrix elements during the separation and purification of U. The resulting precipitates were separated from the high-matrix supernates through centrifugation and were then fully dissolved in 6 M HCl. After evaporation to dryness, the samples were re-dissolved in 3 M $HNO_3$ and loaded onto pre-cleaned heat shrink Teflon columns containing UTEVA resin (Eichrom Technologies, USA). Uranium separation and purification was achieved following previously published protocols (20, 21, 23, 65, 66). Samples were evaporated to dryness and oxidised using $H_2O_2$ + $HNO_3$ for 24 hrs, to eliminate any organic residues from the resin, then evaporated once more. The purified U fractions were re-dissolved in 0.25 M HCl + 0.05 M HF in preparation for U isotope analysis. Uranium yields were typically > 95% and the total procedural blank was approximately 10–20 pg, which is negligible for U sample sizes of between 30 to 150 ng.

***Uranium-Isotope Analysis.*** Uranium isotopic measurements were performed by multiple collector ICP-MS (MC-ICPMS) using a Nu-Plasma HR MC-ICPMS (Nu Instruments, UK) coupled to a DSN-100 desolvation system, at the Centre for Trace Element Analysis, University of Otago, following previously published procedures (22, 23, 66). The $^{238}U/^{235}U$ composition is presented in delta-notation (δ) following Eq. (1).

$$\delta^{238}\mathrm{U} = \left(\frac{(^{238}\mathrm{U}/^{235}\mathrm{U})_{\mathrm{sample}}}{(^{238}\mathrm{U}/^{235}\mathrm{U})_{\mathrm{CRM-145}}} - 1\right) \times 1000 \quad (1)$$

The reference material CRM-145 (National Institute of Standards and Technology, U.S.A.) is the internationally recognized δ-zero standard (19) with a $^{238}U/^{235}U$ ratio of 137.837 ± 0.015. Each sample $\delta^{238}U$ value was calculated relative to two bracketing CRM145 standards, double spiked in the same way as samples, and with ion beam intensities matched to within 10%. Analytical uncertainties are given as twice the standard error (2SE), and reflect the internal instrumental error in the measurements of the sample and bracketing standards using standard techniques of error propagation (23). On average, 2SE was equivalent to ±0.07%, and is comparable to the external reproducibility (2SD) of repeat measurements of the same sample (21). Analytical performance has been verified previously, based on the analysis of certified reference materials (20-23, 66). Replicate analyses performed on samples within and between sessions showed excellent agreement, within the magnitude of their 2SE analytical uncertainties (Fig. S1).

***Elemental Composition Analysis.*** For spiking purposes and in order to identify diagenetic alteration of samples, aliquots of samples were diluted appropriately and measured for their elemental concentrations by quadrupole ICP-MS at the Centre for Trace Element Analysis, University of Otago,

New Zealand. Suitable dilutions of a NIST traceable multi-element standard (Choice Analytical Pty Ltd, Australia) was used for instrumental calibration purposes, and an internal standard comprising a cocktail of 7 reference elements was added to all samples to correct for instrumental drift during measurement. The performance of the elemental analysis methods was checked by analysis of samples spiked with elements of interest. Average recoveries of 102 ± 4% were obtained for the elements reported here. In addition to spiked samples the ICP-MS method has been validated by analysis of digested Basalt, Columbia River (BCR-2) and Basalt, Hawaiian Volcanic Observatory (BHVO-2) certified reference materials (USGS), recoveries averaged 99% ± 5%. A change in digestion protocol from 0.5 to 1M Sodium Acetate may have introduced variability in the U/Ca data, but does not affect the measured $\delta^{238}U_{carb}$. To minimise this effect, secular trends in elemental concentrations for Eastbourne and Raia del Pedale are identified using elemental composition data produced in a previously published study (35) where 5 mg powders were digested using 2 ml of 0.5 M acetic acid. Measurements were made using a Thermo Scientific Element 2 ICP-MS at the University of Oxford.

**Regression Analysis**

To capture the main features of the $\delta^{238}U_{carb}$ dataset at Eastbourne, without placing undue emphasis on single outlying data points, a LOESS smoothing function has been applied to the U-isotope dataset (Fig. 1 and 2). This was performed using the 'ggplot2' package in R, with the 'geom_smooth' function, a default polynomial setting of 2, and $\alpha$=0.15. This also calculates the 95% confidence interval of the LOESS regression. The majority of data points overlap with the 95% confidence interval of this regression (grey shading Fig. 1 and 2), if their analytical uncertainties are taken into account, suggesting that robust systematic trends can be identified. A smoothing function is not appropriate for the Raia del Pedale and South Ferriby datasets due to their lower sampling density and stratigraphic resolution.

**Model Description.**

**Summary.** The model is a simplified version of the GEOCARB and COPSE family of models (11, 13, 49-51), focusing on the shorter term carbon cycle processes. Normalized forcing parameters are: degassing (D) (linked to seafloor spreading rate), uplift driving erosion (E), and effects of vegetation and lithology on weatherability (W). The model is perturbed by an atmospheric $CO_2$ emission from LIP volcanism and calculates the response of the C, P and U cycles (Fig. S2). Briefly, silicate weathering responds to temperature and acts as a sink of C through carbonate burial, and a source of P and U to the ocean. Organic matter production is dependent on P concentrations, and acts as a sink for P and C. The extent of oceanic anoxia is controlled by $O_2$ supply and $O_2$ consumption through the remineralization of organic matter. Anoxic sediments act as a sink for U and C. P concentrations are also influenced by the extent of anoxia due to the redox sensitive burial of Fe-bound and organic-bound P. The U-isotope mass balance is then used to trace the extent of seafloor anoxia and the C-isotope mass balance to trace the relative proportion of organic C burial.

**Carbon and phosphorus cycles.** The model considers both inorganic and organic parts of the carbon cycle. The mass balance for the ocean-atmosphere reservoir of inorganic carbon (A) is given by:

$$dA/dt = F_d - F_w + F_{ox} - F_{morg} - F_{torg} (+ F_{cw} - F_{cb}) + F_{LIP} \quad (2)$$

where the carbon fluxes are $F_d$ = degassing at seafloor spreading centres, $F_w$ = silicate weathering (followed by carbonate burial), $F_{ox}$ = input of organic carbon from oxidative weathering and degassing, $F_{morg}$ = marine-derived organic-carbon burial, and $F_{torg}$ = terrestrially derived organic-carbon burial. Carbonate weathering, $F_{cw}$ is assumed to be balanced by a corresponding carbonate burial flux, $F_{cb}$ (i.e. $F_{cb}=F_{cw}$) so these terms do not affect the dynamics. $F_{LIP}$ is an additional carbon input perturbation due to LIP emplacement; $F_{LIP}$ = 0 at present.

For present-day fluxes (in $10^{12}$ molC $yr^{-1}$) the terms $F_d = k_d = 8$, $F_w = k_w = 8$, $F_{ox} = k_{ox} = 9$, $F_{morg} = k_{morg} = 4.5$, $F_{torg} = k_{torg} = 4.5$, and $F_{cb} = F_{cw} = k_c = 16$, based on COPSE (and hence GEOCARB) are assigned. The present-day reservoir $A_0 = 3.2\text{x}10^{18}$ molC, giving a residence time with respect to silicate weathering removal of 400 thousand years (kyr), or with respect to silicate weathering plus organic-carbon burial of 188 kyr.

The degassing flux is given by:

$$F_d = k_d * D \quad (3)$$

The silicate weathering flux is taken to depend on temperature, $CO_2$, uplift, and the effects of vegetation and lithology (e.g. basalts versus granites) on weatherability:

$$F_w = k_w * E * W * f(CO_2) * f(T) \quad (4)$$

Existing models assume that weathering is predominantly biotic by the mid-Cretaceous and therefore $f(CO_2)$ is the response of vegetation (rather than abiotic weathering) to $CO_2$ following Michaelis-Menten kinetics (after GEOCARB III). Here, $CO_2$ concentration is given in PAL, representing multiples of present atmospheric level:

$$f(CO_2) = 2*CO_2/(1+CO_2) \quad (5)$$

The proportion of inorganic carbon that resides in the atmosphere as $CO_2$ scales with total ocean–atmosphere inorganic carbon inventory (A)

$$CO_2 = (A/A_0)^2 \quad (6)$$

The effect of changes in $CO_2$ and solar luminosity on temperature (from GEOCARB III) is:

$$\Delta T = k_{CO2} * \ln(CO_2) - k_{SL} * (t/570) \quad (7)$$

where $k_{CO2}$ = 4°C (corresponding to a present-day climate sensitivity of about 2.8°C for doubling $CO_2$) and $k_{SL}$ = 7.4°C for $t$ in millions of years ago, which gives ~1.2°C cooling at 94 Ma due to lower solar luminosity.

The dependence of weathering on temperature neglects temperature-driven changes in runoff and only considers the kinetic effect of temperature on mineral dissolution, which using an activation energy appropriate for granite is given by:

$$f(T) = \exp(0.09 * \Delta T) \quad (8)$$

The input of organic carbon from oxidative weathering and degassing is kept constant for simplicity (although oxidative weathering depends on uplift and organic-carbon degassing depends on degassing):

$$F_{ox} = k_{ox} \quad (9)$$

Terrestrial-derived organic-carbon burial is assumed to be fertilised by $CO_2$ (consistent with the weathering formulation):

$$F_{torg} = k_{torg} * f(CO_2) \quad (10)$$

Marine-derived organic-carbon burial is taken to depend on ocean phosphorus concentration (normalized to modern values):

$$F_{morg} = k_{morg}*(P/P_0) \quad (11)$$

Thus, to determine marine-derived organic-carbon burial the phosphorus cycle needs to be considered.

Phosphorus weathering is assumed to be tied to silicate weathering:

$$F_{Pw} = k_{Pw}*(F_w/F_{w0}) \quad (12)$$

where $k_{Pw} = 72x10^9$ molP $yr^{-1}$.

The ocean P balance is given by:

$$dP/dt = F_{Pw} - F_{OrgP} - F_{FeP} - F_{CaP} \quad (13)$$

where $F_{OrgP}$ is burial associated with organic matter, $F_{FeP}$ is burial adsorbed to iron oxides, $F_{CaP}$ is burial associated with carbonate minerals. For present day fluxes ($x10^9$ molP $yr^{-1}$) we assign $k_{OrgP} = 18$, $k_{FeP} = 18$, $k_{CaP} = 36$.

Organic phosphorus burial is sensitive to the anoxic fraction of the ocean, $f_{anoxic}$, given very different $(C/P)_{organic}$ burial ratios under anoxic ($CP_{anoxic}$=1000) and oxic ($CP_{oxic}$=250) bottom waters (52):

$$F_{OrgP} = F_{morg}*((f_{anoxic}/CP_{anoxic})+((1-f_{anoxic})/CP_{oxic})) \quad (14)$$

Iron oxide-bound P burial is also sensitive to the anoxic fraction of the ocean:

$$F_{FeP} = k_{FeP}*(1-f_{anoxic}) \quad (15)$$

Calcium-bound phosphorus burial is assumed to scale with P input to sediments from sinking organic matter (with no redox dependence):

$$F_{CaP} = k_{CaP}*(P/P_0) \quad (16)$$

The function defining the fraction of seafloor overlain by anoxic waters, $f_{anoxic}$, adopts a logistic functional form dependent on the balance between normalized oxygen demand ($k_U*(P/P_0)$) and normalized oxygen supply ($O_2/O_{20}$), where $k_U$ represents the efficiency of nutrient utilization in upwelling regions:

$$f_{anoxic} = 1/(1+e^{-kanox*(ku*(P/P0)-(O2/O20))}) \quad (17)$$

Here, $k_U$ = 0.5 is chosen based on observations of high-latitude nutrient utilization and agreement across a range of models (9, 59, 71, 72) that a transition from an oxic to an anoxic deep ocean occurs at $O_2/O_{20}$ ~0.5 PAL (for present nutrient levels), or at $P/P_0$ ~2 (for present $O_2$ levels). $k_{anox}$ = 12 is chosen based on observations that ~0.2–0.3% of the seafloor is overlain by anoxic bottom waters at present (73), and model agreement that the transition from oxic to anoxic conditions is abrupt as, for example, $O_2/O_{20}$ drops from ~0.6 to ~0.4 (9, 59, 72).

We make a simple consideration of the effect of increases in atmospheric $O_2$ by integrating any increases in organic-carbon burial above the initial steady state to give a cumulative input of $O_2$, calculating the resulting change in $O_2/O_{20}$ (where the present $O_{20} = 3.7\text{x}10^{19}$ mol), and feeding this change in $O_2/O_{20}$ back into $f_{anoxic}$. We do not consider longer term negative feedbacks on $O_2$ because of the short interval under consideration here.

**Carbon-isotope mass balance.** The carbon-isotope mass balance follows the carbon mass balance:

$$d(A*\delta_A)/dt = F_d*\delta_d + F_{ox}*\delta_{ox} + F_{cw}*\delta_{cw} + F_{LIP}*\delta_{LIP} - (F_{morg} + F_{torg})*(\delta_A - \Delta) - (F_w + F_{cb}) *\delta_A \quad (18)$$

The above equation can be simplified to:

$$d(A*\delta_A)/dt = F_{in}*\delta_{in} + F_{LIP}*\delta_{LIP} - F_{org}(\delta_A - \Delta) - F_{carb}*\delta_A \quad (19)$$

where $F_{in} = F_d + F_{ox} + F_{cw}$ is the total steady state input flux of carbon of mean isotopic composition $\delta_{in}$ = -5 ‰ (as often assumed in other studies), the carbon input perturbation $F_{LIP}$ has isotopic composition $\delta_{LIP}$ (see sensitivity analysis below), $F_{org} = F_{morg} + F_{torg}$ is the total burial flux of organic matter with fractionation $\Delta$ (taken here to be 25 ‰) and $F_{carb} = F_w + F_{cb}$ is the total burial flux of carbonates (with no assumed C-isotope fractionation).

Simplifying equation (19) in the same manner ($dA/dt = F_{in} + F_{LIP} - F_{org} - F_{carb}$), then applying the product rule ($d(A*\delta_A)/dt = A*d\delta_A/dt + \delta_A*dA/dt$) and substituting and rearranging gives:

$$d\delta_A/dt = (F_{in}*(\delta_{in} - \delta_A) + F_{LIP}*(\delta_{LIP} - \delta_A) - F_{org}*(-\Delta))/A \quad (20)$$

With no perturbation ($F_{LIP}$ = 0) at steady state ($d\delta_A/dt$ = 0) this corresponds to the widely-used formulation:

$$\delta_A = \delta_{in} + f*\Delta \quad (21)$$

Where 'f' is the fraction of carbon buried in organic form i.e. $f = F_{org}/F_{in} = F_{org}/(F_{org} + F_{carb})$. For the modern fluxes suggested above f=9/33=0.273 and $\delta_A$~1.8 ‰ if $\Delta$=25.

**Uranium-isotope mass balance**

The U-cycle model assumes that the riverine input of U is driven by silicate weathering, all U sinks scale linearly with U concentration, the hydrothermal sink of U also scales with degassing from seafloor spreading (D), and the anoxic sink of U also scales with $f_{anoxic}$, the fraction of anoxic seafloor:

$$dU/dt = F_{riv} - F_{hyd} - F_{anoxic} - F_{carbonate} - F_{suboxic} - F_{oxic\ metals} \quad (22)$$

$$F_{riv} = k_{riv}*F_w/F_{w0} \quad (23)$$

$$F_{hyd} = k_{hyd}*D*(U/U_0) \quad (24)$$

$$F_{anoxic} = k_{anoxic}*(U/U_0)*f_{anoxic}/f_{anoxic0} \quad (25)$$

$$F_{carbonate} + F_{suboxic} + F_{oxic\ metals} = F_{other} = k_{other}*(U/U_0) \quad (26)$$

For a modern U=1.85x$10^{13}$ mol, we use estimates of $k_{anoxic}$ = 6.2x$10^6$ mol $yr^{-1}$, $k_{hyd}$ = 5.7x$10^6$ mol $yr^{-1}$, $k_{other}$ = 36x$10^6$ mol $yr^{-1}$, and therefore $k_{riv}$ = 47.9x$10^6$ mol $yr^{-1}$ (16, 19). The corresponding isotope mass balance is:

$$d\delta_U/dt = (F_{riv}*(\delta_{riv} - \delta_U) - F_{hyd}*\Delta_{hyd} - F_{anoxic}*\Delta_{anoxic} - F_{other}*\Delta_{other})/U \quad (27)$$

(Note here that $\Delta$ are all positive for U isotopes, in contrast to $\Delta$ for C isotope fractionation.) For the modern (18, 19, 30, 54) we assume $\delta_{riv}$ = -0.29, $\Delta_{hyd}$ = 0.2, $\Delta_{anoxic}$ = 0.5, and $\delta_U$ = -0.39, requiring $\Delta_{other}$ = 0.0156 for steady state.

**Mid-Cretaceous model initialisation, U cycle assumptions and perturbation scenarios**

***Boundary conditions:*** The mid-Cretaceous had elevated rates of seafloor spreading and corresponding degassing, with D=1.5, as used in GEOCARB/COPSE models. At the time of OAE 2, an increase in hydrothermal input by 20% has been estimated to be consistent with an observed Sr-isotope shift (8, 74) hence we use D=1.8 as the baseline value. Uplift was considerably lower in the mid-Cretaceous than at present, with E=0.7 from GEOCARB/COPSE used as a baseline. The rise of angiosperms is assumed to have finished increasing weathering rates by 100 Ma, following GEOCARB/COPSE. Basalt area is estimated to be comparable to today (75). Therefore, present weatherability W = 1 is used as a baseline. Lower solar luminosity at 94 Ma translates to 1.2°C of cooling. Higher steady-state atmospheric $O_2$ is considered as part of our sensitivity analysis.

***U Isotope Fractionation Factor***: The sensitivity of changes in calculated $\delta^{238}U_{sw}$, in terms of reflecting the degree of anoxia, is dependent on the assumed magnitude of fractionation during U reduction between anoxic sediments and seawater ($\Delta_{anoxic}$). Modern observational, theoretical and experimental data suggest that the reduction of U(VI) to U(IV) is associated with a positive U-isotope fractionation factor of between 0.4 to 1.3 ‰ (14, 19, 20, 23-25, 30, 76) where the apparent enrichment factor in natural settings may be highly variable and dependent on local geochemical and depositional conditions (18, 20, 30), which are hard to quantify on a global scale during Earth's history. To this end, previous mass balance models for the Permo-Triassic mass extinction and OAE 2 have employed various enrichment factors of +0.5 (14, 26), +0.6 (28) and +0.77 ‰ (29), which generate significantly different estimates for the size of anoxic sinks, and hence seafloor area covered by anoxic waters, required to drive a given negative $\delta^{238}U$ excursion. The assumption of $\Delta_{anoxic}$ remains a fundamental limitation for the interpretation of ancient $\delta^{238}U$ data. Due to this uncertainty, we use the observed difference in $\delta^{238}U$ between contemporaneous anoxic shales (ODP site 1261, Fig. 1) where the average post-OAE value reported for ODP 1262 is 0.063‰ (14) and Eastbourne is -0.45‰, giving a $\Delta_{anoxic}$ of +0.51‰, which is within the range of observational data from modern anoxic basins (14, 19, 20, 23-25, 30, 76). Sensitivity analysis (Table S2) demonstrates that increasing $\Delta_{anoxic}$ to 0.6‰, would increase the magnitude of the negative $\delta^{238}U_{sw}$ excursion by 0.1‰ for the same $CO_2$ emission scenario and size of anoxic sinks. To match the observed excursions in Eastbourne when $\Delta_{anoxic}$ = 0.6‰ then requires a decrease in the perturbation magnitude, and lower estimates of the area of seafloor anoxia of 4 to 10%. If $\Delta_{anoxic}$ were assumed to be much larger this drives the steady state $\delta^{238}U_{sw}$ lower than the range recorded at Eastbourne and is not deemed plausible without invoking unrealistically high $\delta_{riv}$ values, or invoking a diagenetic offset for which there is no evidence. It would also require smaller changes to the carbon cycle model, with a smaller $CO_2$ emission, temperature increase and relative change in productivity, in order to drive the same magnitude of $\delta^{238}U$ excursion. The result of this would be to decrease the amount of carbon removed from the ocean-atmosphere system through productivity and burial under anoxic conditions, and therefore create a decrease in the magnitude of the calculated positive CIE. Using a $\Delta_{anoxic}$ of +0.5‰ generates a good agreement between the model outputs for temperature and estimates from proxy reconstructions, and produces a $\delta^{13}C$ excursion that is only ~0.5‰ lower than observed at Eastbourne. Thus we do not consider the higher fractionation factor/smaller perturbation scenario to be realistic for OAE 2. The internally consistent carbon cycle model therefore helps increase the confidence in our interpretation of the area of seafloor that was overlain by an anoxic water column.

***U riverine input:*** The modern average measured riverine $\delta^{238}U$ composition ($\delta_{riv}$) is indistinguishable from bulk silicate earth (BSE) at -0.29‰ (18, 19, 21, 54, 69, 77). In the mid-

Cretaceous setup of the C–P–U model (see below), $\delta_{riv}$ is set to ~ -0.19‰ in order to generate $\delta^{238}U_{sw}$ values in agreement with the $\delta^{238}U_{carb}$ data from Eastbourne under different atmospheric $O_2$ scenarios. Although this value is slightly higher than modern average $\delta_{riv}$ it is a plausible figure given the uncertainty of exposed weatherable lithologies on land. Indeed, it has been suggested that $\delta_{riv}$ could vary by up to a few per mil for different periods of Earth's history (28) although estimates are limited by substantial uncertainties including the paleogeology reconstructions, degree of soil development, vegetation cover and changing weathering regimes. The chosen value used here for $\delta_{riv}$ is also within the range back-calculated through mass-balance modelling of the modern U cycle ($\delta_{riv}$ = -0.18 to -0.28 ‰), which encompasses the uncertainty of the size and isotopic composition of modern U sinks (19). Thus, using either the modern $\delta_{riv}$ that is close to BSE, or a slightly higher $\delta_{riv}$ of -0.19 ‰ makes little difference within the uncertainty of the current characterization of U sinks.

***Resulting steady state:*** With these changes in boundary conditions (at $O_2$ =1) the predicted $A/A_0$ = 1.63, $CO_2$ = 2.7 PAL and $\Delta T$ = +2.7°C (i.e. global average T ~ 18°C), comparing well with GEOCARB III and the warmer world at the time. Predicted $P/P_0$ = 1.43, which assuming present $O_2$ generates more anoxia ($f_{anoxic}$ = 0.03). $\delta^{13}C$ ~ +3.2 ‰ is predicted thanks to elevated terrestrial and marine organic-carbon burial (consistent with data from Eastbourne and South Ferriby). These changes in boundary conditions lead to a predicted increase in U river input outweighed by an increase in the anoxic sink, leading to a predicted decrease in ocean U content to $0.9x10^{13}$ mol (50% of present), and when $\delta_{riv}$ = -0.19 and $\Delta_{anoxic}$ = 0.5 this gives a predicted $\delta_U$ = -0.53 ‰.

***LIP $CO_2$ injection:*** A carbon cycle perturbation associated with the emplacement of the Caribbean-Columbian, Madagascar and/or other LIPs close to the Cenomanian/Turonian boundary has been hypothesized as the trigger for OAE 2. These two LIPs are each estimated at $4.5x10^6$ $km^3$ basalt (78) equivalent to mass $1.3x10^7$ Gt (density 2.9 g $cm^{-3}$) that, assuming 2.0 wt% $CO_2$ (79), yields $2.6x10^5$ $GtCO_2$ or $7.1\times10^4$ GtC or $5.91x10^{18}$ molC. This figure gives a combined total carbon pool that could be degassed throughout the emplacement of these two LIPs of ~$12x10^{18}$ molC. The nature and corresponding rate of degassing is uncertain. We consider release events of ~10–20% of the total as plausible (i.e. 1.2–$2.4x10^{18}$ molC), which over 150 kyr amounts to 0.8–$1.6x10^{13}$ molC $yr^{-1}$, up to a doubling of the degassing flux. Clearly multiple perturbations of approximately this magnitude could have occurred during the full interval of LIP emplacement.

If the prescribed $CO_2$ injection is assumed to be solely mantle derived with a $\delta^{13}C$ signature of -5‰, then a minor negative CIE (of ~1‰) before the positive CIE of OAE 2 is predicted (Table 2). However, there is little indication of this feature in the $\delta^{13}C$ record for OAE 2, unlike other similar events such as the early Aptian OAE 1a (~120 Ma) (1), suggesting either a slower initial rate of $CO_2$

emission for OAE 2, where the potential negative excursion was counterbalanced by the burial of organic matter, or that the degassed volatiles contained a mixture of mantle-derived and assimilated carbonate C from overlying crustal material. Because of this potential complication, the injected carbon is assumed to have a $\delta^{13}C$ signature of 0‰ in the model runs shown in Fig. 3. Due to the inherent delay in the carbon cycle between the timing of the $CO_2$ injection and maximum extent of oceanic anoxia, the maximum $\delta^{13}C$ predicted for the subsequent positive CIE is less sensitive to this assumed input $CO_2$ signature, with only ~0.1‰ difference between the two scenarios (Table S2).

***Sensitivity analyses.*** A series of sensitivity analyses show that decreasing background $CO_2$ degassing (D), uplift and erosion rates (E), or the weatherability of exposed landmasses (W), leads to reduced levels of anoxia during the pre-OAE 2 interval and therefore higher predicted values of $\delta^{238}U_{sw}$. Such boundary conditions make the calculated changes in anoxia, [U], $\delta^{238}U_{sw}$ and $\delta^{13}C$ less sensitive to the same $CO_2$ perturbation. Importantly, for reasonable initial boundary conditions that are consistent with more complex biogeochemical models, geologically plausible magnitudes of $CO_2$ increases can drive expanded anoxia, and inferred $\delta^{238}U_{sw}$ changes in all cases. In a first set of model sensitivity analyses (Table S1) we vary the model boundary conditions of D, E, W, and atmospheric $O_2$ over plausible ranges. We consider D=1.5 as a lower limit (no extra increase in hydrothermal activity) and D=2.1 (symmetric perturbation) as an upper limit. E is varied over ±0.2, which spans most of the Phanerozoic range (13). W is varied over ±0.2 given uncertainty in the effect of angiosperms on weathering and in the background area of volcanic rocks at the time (75). For atmospheric $O_2$ following recent work (53) we only consider increases and we limit these to a level (1.2 PAL) that returns modern levels of ocean anoxia (given evidence for more widespread anoxia prior to OAE2). These changes in boundary conditions alter the initial steady state and the core dynamics of the model, and we examine how this changes the response to a common $CO_2$ injection perturbation of $1.8x10^{18}$ molC over 150 kyr ($1.2x10^{13}$ molC/yr). In a second set of sensitivity analyses (Table S2) we take the same perturbation experiment from standard boundary conditions with $O_2$ = 1 PAL and vary the assumed $\delta^{13}C$ of LIP $CO_2$ input, and $\delta_{riv}$ and $\Delta_{anoxic}$ in the U isotope system. These changes only affect the isotopic expression of the modelled C, P, U changes.

**SI Discussion**

Primary biotic and abiotic calcite and aragonite precipitates have been shown to record ambient solution $\delta^{238}U$ values accurately with minimal fractionation, despite structural co-ordination changes with regard to calcite precipitation (21, 25, 31, 32). These studies also suggest that there is no appreciable fractionation driven by biotic 'vital effects', consistent with the fact that U does not serve a biological function. A minor positive fractionation factor has been observed for abiotic aragonite formation under very specific experimental conditions, whereby the solid phase has a more positive

930 $\delta^{238}U$ than the residual solution (32) although the applicability of these experimental results to real-
931 world conditions is still not well understood. This complication could only have potentially effected
932 Raia del Padale, which was originally comprised of mixed aragonite and calcite that is typical of
933 shallow-water platform settings. U concentrations are also vastly different between calcite and
934 aragonite, with aragonite being up to two orders of magnitude greater. This difference is clearly seen
935 in the greater U/Ca ratios of the Raia del Pedale carbonates (Fig. 1) and the mixed mineralogy of this
936 section could also explain the greater degree of scatter. Despite this the general trends in U/Ca are
937 replicated at the two sites.
938 Diagenesis is an important consideration for understanding any geochemical dataset,
939 especially in carbonates that can undergo extensive syn- and post-depositional recrystallization. The
940 redox-sensitive nature of U also introduces additional complications in the diagenetic environment. U
941 mobility in sediments is heavily influenced by local reduction and diffusion within pore waters (18, 31,
942 80) and secondary U can be incorporated into diagenetic cements or into neomorphosed carbonates
943 (31, 81). This process has been demonstrated for individual carbonate cements (81) and for bulk
944 samples from modern carbonate cores which tend to show a positive $\delta^{238}U$ offset compared to
945 contemporary seawater (31). Negative $\delta^{238}U$ offsets have also been measured in some dolomitized
946 carbonates (21, 31). The reason for this is poorly understood but it may be due to either the influence
947 of meteoric waters with more negative $\delta^{238}U$ signatures, or alteration under hypersaline conditions
948 (21, 31).
949 The influence of pore-water reduction and syn-sedimentary recrystallization or cementation
950 should be lowest in the Eastbourne Chalk section, which is thought to have had an oxygenated water
951 column during deposition, with very low total organic carbon (TOC; less than 0.15% (82)) and no
952 appreciable sulphate reduction in pore waters (33). The impact of later stage diagenesis should be
953 minimal at Eastbourne, with the stable low-magnesium calcite mineralogy characteristic of pelagic
954 calcifiers that is more resistant to diagenetic alteration (83). This supposition is confirmed by the lack
955 of correlation between $\delta^{238}U$ with [U] or Mn/Ca and Sr/Ca (Fig. S3). Indeed, Eastbourne has been
956 widely used as a reference section for many isotopic systems because of the exemplary nature of the
957 archive. It is encouraging that major changes in $\delta^{238}U$ are not dependent on lithology, and also cross
958 major lithology transitions. In general the $\delta^{238}U_{carb}$ data during the OAE 2 interval show systematic
959 trends that correspond to hypothesised changes in other environmental parameters. Preceding the
960 CIE of OAE 2, however, is a negative $\delta^{238}U_{carb}$ excursion that corresponds to a U/Ca decrease. We do
961 not focus on this excursion, however it is plausibly related to observed cyclic black shales that precede
962 OAE 2 and thought to represent anoxia driven by orbital variability (68).

963 Carbonate samples from South Ferriby also show little geochemical evidence for
964 recrystallization (Fig. S3) although the section is generally more lithified than Eastbourne. The
965 presence of the distinct black shale (the so-called 'Black Band') above the unconformity raises some
966 concerns. Potentially, U mobilization from the organic-rich level could explain the positive $\delta^{238}U$
967 excursion seen in South Ferriby. The highest $\delta^{238}U_{carb}$ in this section also correspond to the highest
968 Mn/Ca ratios, suggesting the influence of pore water U reduction.
969 In contrast to the pelagic sites, Raia del Pedale has undergone extensive recrystallization, with
970 evidence for interaction with meteoric waters coming from depleted Sr/Ca and, in places, high Mg/Ca
971 indicative of dolomitization. In particular, the three lowest $\delta^{238}U$ values in Raia del Pedale are from
972 samples with higher Mg/Ca and anomalously high U/Ca ratios (Fig. 1, Fig. S3), consistent with an
973 observed negative isotopic shifts between modern dolomites and seawater (21, 31). These low values
974 however, form a negative excursion that appears to correlate with the Eastbourne $\delta^{238}U_{carb}$ data
975 during the more variable pre-OAE 2 interval (Fig. 1). Further investigation of pre-OAE 2 U-isotopes are
976 required to test if this excursion is primary. The anomalously high $\delta^{238}U_{carb}$ values within the OAE 2
977 interval at Raia del Pedale are more typical of signatures found in anoxic shales and may potentially
978 indicate extensive early diagenetic alteration and secondary incorporation of U from *in situ* organic-
979 matter degradation. Interestingly, Mn is not enriched in these samples, as would be expected due to
980 alteration under reducing pore waters. These high $\delta^{238}U_{carb}$ values are, however, restricted to a few
981 samples only, suggesting that these potential geochemical impacts were probably spatially limited.
982

**Supplementary Figures**

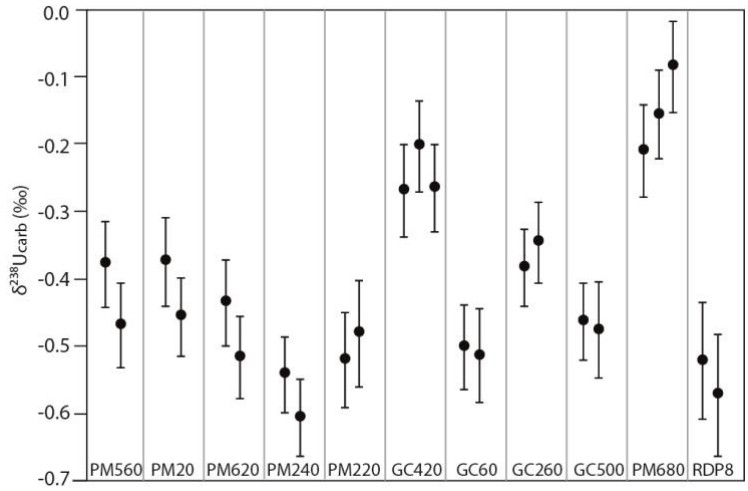


Fig. S1: Replicate measurements performed on multiple samples between analysis sessions. Uncertainty shown as 2 SE.

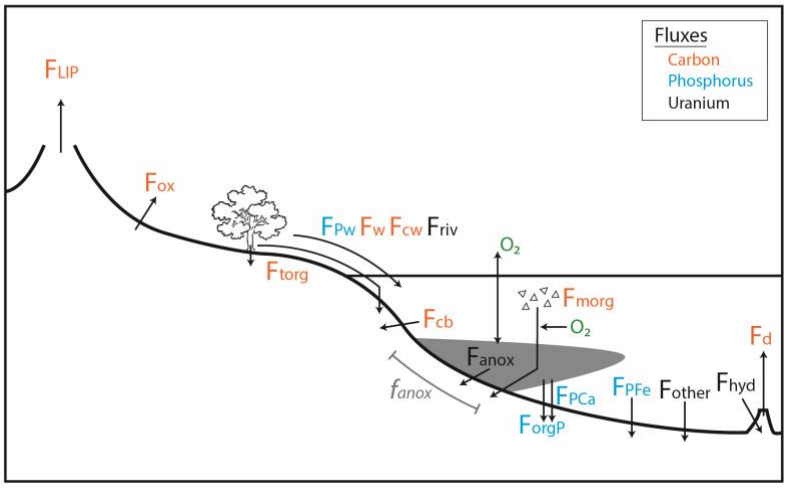


Fig. S2. Schematic illustrating coupled model fluxes of the C–P–U cycles with reference to the variables defined in the text.

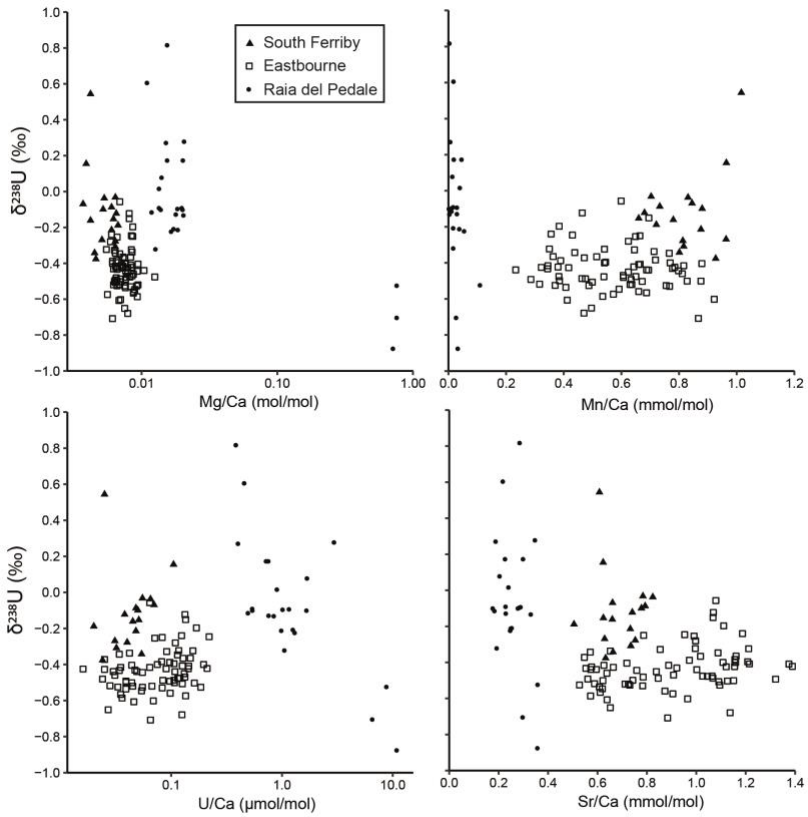


995

996 Fig. S3: Cross plots of $\delta^{238}U$ against geochemical indicators of diagenesis.

997

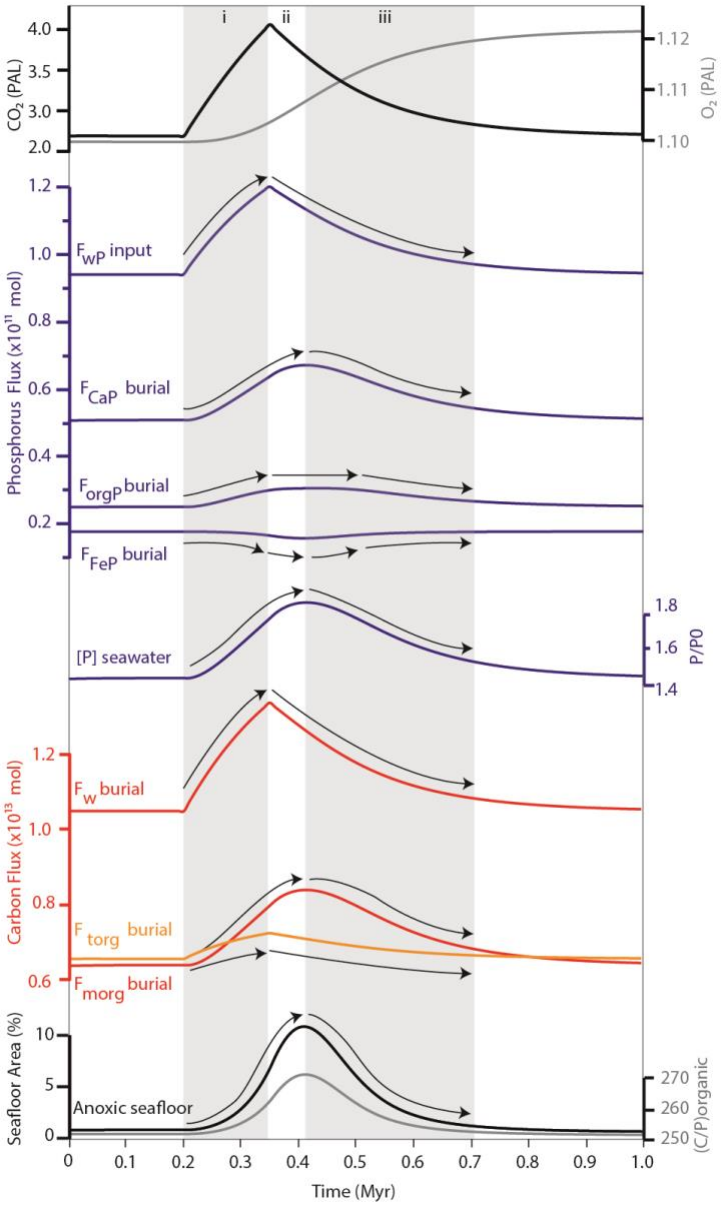


998

999 Fig. S4: C–P–U model outputs for a single expansion of anoxia under the $0_2$ = 1.1 scenario with a $CO_2$
1000 emission of $1.05 \times 10^{13}$ mol C $yr^{-1}$ for 150 kyrs. See model description and main text for element flux
1001 symbols. The behaviour of the C and P cycles can be divided into three stages related to the
1002 development of anoxia: i) the onset of deoxygenation; ii) peak extent of anoxia; and iii)
1003 reoxygenation. C and P fluxes are separated and the arrows highlight the behaviour of each flux
1004 across the three stages. Specifically, a decoupling of [P] and P inputs ($F_{wP}$) in stage (ii) is related to
1005 changes in the C/P ratio and burial of organic bound P ($F_{orgP}$) and Fe bound P ($F_{FeP}$). The minor
1006 increase in atmospheric $O_2$, due to the burial of organic carbon, is also shown. These internal P
1007 dynamics create the delay in the maximum extent of anoxia compared to the atmospheric $CO_2$
1008 increase and also facilitate reoxygenation as $CO_2$ decreases.

1009

1010

**Table S1. Sensitivity analysis varying the model boundary conditions** (with a common 1.8x10$^{18}$ molC perturbation over 150 kyr with $\delta_{LIP}$ = 0 ‰). Boxed rows highlight boundary conditions used in the main text.

| Initial conditions | | | | Initial steady-state outputs | | | | | | Maximum excursion outputs | | | | | |
|---|---|---|---|---|---|---|---|---|---|---|---|---|---|---|---|
| D | E | W | $O_2/O_{20}$ | $CO_2$ | $P/P_0$ | $U/U_0$ | $f_{anoxic}$ | $\delta^{13}C$ | $\delta_U$ | $CO_2$ | $P/P_0$ | $U/U_0$ | $f_{anoxic}$ | $\delta^{13}C$ | $\delta_U$ |
| 1 | 1 | 1 | 1 | 1 | 1 | 1 | 0.003 | 1.82 | *-0.39** | 1.82 | 1.69 | 0.35 | 0.12 | 3.82 | *-0.87** |
| 1.8 | 0.7 | 1.0 | 1.0 | 2.68 | 1.43 | 0.50 | 0.031 | 3.23 | -0.53 | 4.26 | 2.45 | 0.03 | 0.92 | 5.54 | -1.01 |
| 1.8 | 0.7 | 1.0 | 1.1 | 2.69 | 1.42 | 0.91 | 0.009 | 3.21 | -0.39 | 4.28 | 1.95 | 0.20 | 0.17 | 4.35 | -0.88 |
| 1.8 | 0.7 | 1.0 | 1.2 | 2.69 | 1.41 | 1.18 | 0.003 | 3.20 | -0.30 | 4.29 | 1.89 | 0.78 | 0.04 | 4.22 | -0.52 |
| 1.5 | 0.7 | 1.0 | 1.0 | 2.24 | 1.22 | 0.82 | 0.009 | 2.91 | -0.39 | 3.53 | 1.68 | 0.27 | 0.12 | 4.19 | -0.89 |
| 2.1 | 0.7 | 1.0 | 1.0 | 3.12 | 1.67 | 0.20 | 0.120 | 3.57 | -0.63 | 4.79 | 2.86 | 0.03 | 0.99 | 6.00 | -0.87 |
| 1.8 | 0.5 | 1.0 | 1.0 | 4.42 | 1.35 | 0.63 | 0.019 | 3.50 | -0.47 | 6.63 | 1.76 | 0.15 | 0.18 | 4.34 | -0.85 |
| 1.8 | 0.9 | 1.0 | 1.0 | 1.92 | 1.49 | 0.40 | 0.046 | 3.02 | -0.56 | 3.14 | 2.74 | 0.03 | 0.99 | 5.77 | -1.01 |
| 1.8 | 0.7 | 0.8 | 1.0 | 3.70 | 1.37 | 0.59 | 0.023 | 3.41 | -0.49 | 5.68 | 1.90 | 0.08 | 0.33 | 4.53 | -0.93 |
| 1.8 | 0.7 | 1.2 | 1.0 | 2.10 | 1.47 | 0.43 | 0.041 | 3.08 | -0.55 | 3.41 | 2.67 | 0.03 | 0.98 | 5.73 | -1.01 |

*Note: U-isotope system set up for the modern with $\delta_{riv}$ -0.29. All other scenarios assume $\delta_{riv}$ -0.19

1011

1012

1013

**Table S2. Sensitivity analysis varying the model isotopic assumptions.** Using standard boundary conditions of D=1.8, E=0.7, W=1.0, $O_2$=1.0, and a common 1.8x$10^{18}$ molC perturbation over 150 kyr.

| Input assumptions | | | $\delta^{13}C$ | | | $\delta^{238}U_{sw}$ | | | |
|---|---|---|---|---|---|---|---|---|---|
| $\delta^{13}C$ LIP | $\delta^{238}U_{river}$ | $\Delta_{anoxic}$ | initial | min | max | initial | min | max | Final |
| **-5** | | | 3.23 | 2.26 | 5.41 | | | | |
| **0** | | | 3.23 | 2.96 | 5.54 | | | | |
| **-10** | | | 3.23 | 1.44 | 5.29 | | | | |
| | **-0.19** | **0.5** | | | | -0.53 | -1.01 | -0.31 | -0.48 |
| | **-0.29** | 0.5 | | | | -0.63 | -1.11 | -0.41 | -0.58 |
| | **-0.09** | 0.5 | | | | -0.43 | -0.91 | -0.21 | -0.38 |
| | -0.19 | **0.4** | | | | -0.46 | -0.85 | -0.29 | -0.43 |
| | -0.19 | **0.6** | | | | -0.59 | -1.17 | -0.33 | -0.53 |

1014

1015

**Data Tables**

| Eastbourne U-isotope data and trace element ratios performed on 0.6 or 1 M Sodium Acetate leachates. Li-isotope data after ref 8 and this study. Heights from base of section. | | | | | | | | | |
|---|---|---|---|---|---|---|---|---|---|
| Sample Name | Height (cm) | $\delta^{238}$Ucarb (‰) | 2SE | Mg/Ca (mol/mol) | Sr/Ca (mmol/mol) | Mn/Ca (mmol/mol) | U/Ca (µmol/mol) | δ7Li (‰) | 2SD |
| GC600 | 0 | -0.559 | 0.065 | 0.009 | 0.873 | 0.660 | 0.098 | | |
| GC580 | 20 | -0.477 | 0.057 | 0.008 | 1.045 | 0.539 | 0.115 | | |
| GC560 | 40 | -0.366 | 0.057 | 0.008 | 1.017 | 0.514 | 0.128 | | |
| GC540 | 60 | -0.197 | 0.085 | 0.009 | 1.111 | 0.384 | 0.169 | | |
| GC500 | 100 | -0.470 | 0.071 | 0.009 | 0.908 | 0.606 | 0.133 | 19.1 | 0.6 |
| GC460 | 140 | -0.123 | 0.057 | 0.008 | 1.069 | 0.464 | 0.133 | | |
| GC440 | 160 | -0.451 | 0.066 | 0.008 | 0.838 | 0.624 | 0.131 | | |
| GC420 | 180 | -0.246 | 0.068 | 0.008 | 0.953 | 0.430 | 0.220 | | |
| GC400 | 200 | -0.488 | 0.068 | 0.008 | 0.846 | 0.475 | 0.084 | 20.3 | 0.2 |
| GC380 | 220 | -0.679 | 0.048 | 0.008 | 1.137 | 0.470 | 0.125 | | |
| GC360 | 240 | -0.476 | 0.063 | 0.008 | 1.064 | 0.383 | 0.120 | | |
| GC300 | 300 | -0.487 | 0.059 | 0.007 | 1.067 | 0.463 | 0.106 | 19.2 | 0.9 |
| GC260 | 340 | -0.365 | 0.057 | 0.007 | 1.161 | 0.363 | 0.149 | | |
| GC200 | 400 | -0.423 | 0.068 | 0.007 | 1.155 | 0.380 | 0.143 | | |
| GC160 | 440 | -0.388 | 0.065 | 0.006 | 0.972 | 0.389 | 0.097 | | |
| GC120 | 480 | -0.323 | 0.065 | 0.006 | 0.996 | 0.350 | 0.117 | | |
| GC100 | 500 | -0.240 | 0.087 | 0.006 | 1.187 | 0.356 | 0.124 | 23.9 | 0.1 |
| GC60 | 540 | -0.507 | 0.069 | 0.006 | 1.091 | 0.499 | 0.126 | | |
| GC40 | 560 | | | | | | | **20.6** | **0.4** |
| GC00 | 600 | -0.280 | 0.052 | 0.006 | 0.997 | 0.624 | 0.109 | 11.2 | 0.5 |
| PM20 | 620 | -0.416 | 0.059 | 0.006 | 0.888 | 0.816 | 0.064 | | |
| PM40 | 640 | -0.328 | 0.059 | 0.006 | 0.854 | 0.645 | 0.091 | | |
| PM60 | 660 | -0.526 | 0.066 | 0.009 | 1.095 | 0.755 | 0.185 | **11.9** | **0.0** |

| | | | | | | | | | |
|---|---|---|---|---|---|---|---|---|---|
| PM100 | 700 | | | | | | | 7.4 | 0.7 |
| PM120 | 720 | -0.400 | 0.071 | 0.008 | 1.159 | 0.541 | 0.196 | | |
| PM140 | 740 | -0.503 | 0.067 | 0.007 | 1.126 | 0.672 | 0.162 | | |
| PM180 | 780 | -0.347 | 0.060 | 0.007 | 1.088 | 0.766 | 0.114 | | |
| PM200 | 800 | | | | | | | **8.7** | **0.1** |
| PM220 | 820 | -0.501 | 0.070 | 0.006 | 1.151 | 0.876 | 0.107 | | |
| PM240 | 840 | -0.574 | 0.057 | 0.006 | 0.905 | 0.572 | 0.135 | | |
| PM260 | 860 | -0.602 | 0.068 | 0.007 | 0.965 | 0.922 | 0.069 | | |
| PM280 | 880 | -0.708 | 0.060 | 0.006 | 0.884 | 0.867 | 0.065 | | |
| PM300 | 900 | -0.408 | 0.065 | 0.007 | 1.215 | 0.665 | 0.126 | 5.9 | 0.4 |
| PM340 | 940 | -0.400 | 0.071 | 0.006 | 1.108 | 0.769 | 0.075 | **10.7** | **0.3** |
| PM360 | 960 | -0.057 | 0.092 | 0.007 | 1.079 | 0.599 | 0.064 | | |
| PM400 | 1000 | -0.431 | 0.058 | 0.006 | 0.921 | 0.777 | 0.047 | 9.9 | 0.6 |
| PM420 | 1020 | -0.324 | 0.080 | 0.008 | 1.212 | 0.541 | 0.157 | | |
| PM440 | 1040 | -0.396 | 0.064 | 0.007 | 1.208 | 0.545 | 0.106 | | |
| PM480 | 1080 | -0.254 | 0.060 | 0.007 | 0.991 | 0.649 | 0.071 | | |
| PM500 | 1100 | -0.409 | 0.060 | 0.008 | 1.375 | 0.660 | 0.144 | 15.3 | 0.4 |
| PM520 | 1120 | -0.384 | 0.059 | 0.006 | 1.156 | 0.718 | 0.082 | | |
| PM540 | 1140 | -0.493 | 0.061 | 0.008 | 1.321 | 0.634 | 0.097 | | |
| PM560 | 1160 | -0.424 | 0.063 | 0.007 | 1.121 | 0.785 | 0.090 | **13.1** | **0.4** |
| PM580 | 1180 | -0.422 | 0.082 | 0.008 | 1.389 | 0.643 | 0.211 | | |
| PM600 | 1200 | | | | | | | 8.3 | 0.5 |
| PM620 | 1220 | -0.476 | 0.061 | 0.012 | 1.026 | 0.650 | 0.117 | 10.2 | 0.4 |
| PM640 | 1240 | -0.440 | 0.082 | 0.010 | 1.002 | 0.694 | 0.108 | 22.8 | 0.4 |
| PM680 | 1280 | -0.151 | 0.068 | 0.008 | 1.068 | 0.695 | 0.135 | | |
| PM720 | 1320 | -0.404 | 0.068 | 0.009 | 0.719 | 0.879 | 0.044 | | |
| PM740 | 1340 | -0.250 | 0.060 | 0.009 | 0.787 | 0.664 | 0.083 | | |
| PM760 | 1360 | -0.444 | 0.067 | 0.009 | 0.759 | 0.798 | 0.055 | **22.5** | **0.1** |

| | | | | | | | | | |
|---|---|---|---|---|---|---|---|---|---|
| WC0 | 1390 | -0.520 | 0.101 | 0.009 | 0.725 | 0.630 | 0.067 | 20.9 | 0.2 |
| PM800 | 1400 | -0.530 | 0.075 | 0.008 | 0.783 | 0.767 | 0.083 | | |
| W0.2 | 1410 | | | | | | | **21.8** | **0.2** |
| WC200 | 1440 | | | | | | | 17.7 | 0.7 |
| W0.6 | 1450 | -0.546 | 0.071 | 0.009 | 0.620 | 0.592 | 0.054 | | |
| W0.8 | 1470 | | | | | | | | |
| W1 | 1490 | -0.460 | 0.069 | 0.009 | 0.638 | 0.811 | 0.031 | 15.7 | 0.5 |
| W1.2 | 1510 | | | | | | | **13.1** | **0.2** |
| W1.4 | 1530 | -0.566 | 0.069 | 0.009 | 0.611 | 0.687 | 0.035 | | |
| WC300 | 1540 | | | | | | | 14.5 | 0.6 |
| W1.6 | 1550 | -0.439 | 0.071 | 0.008 | 0.595 | 0.687 | 0.030 | | |
| W2 | 1590 | -0.337 | 0.065 | 0.008 | 0.652 | 0.713 | 0.042 | 17.8 | 0.2 |
| W2.4 | 1630 | -0.586 | 0.075 | 0.009 | 0.572 | 0.535 | 0.036 | | |
| W2.8 | 1670 | -0.481 | 0.074 | 0.006 | 0.785 | 0.607 | 0.024 | | |
| W3 | 1690 | | | | | | | 22.5 | 0.3 |
| W3.2 | 1710 | -0.520 | 0.066 | 0.006 | 0.712 | 0.636 | 0.045 | | |
| W3.6 | 1750 | -0.501 | 0.077 | 0.007 | 0.622 | 0.828 | 0.044 | | |
| W4 | 1790 | -0.526 | 0.084 | 0.007 | 0.731 | 0.487 | 0.055 | 20.7 | 0.6 |
| W4.4 | 1830 | -0.499 | 0.073 | 0.007 | 0.743 | 0.385 | 0.039 | | |
| WC600 | 1840 | | | | | | | 23.8 | 0.6 |
| W4.8 | 1870 | -0.651 | 0.078 | 0.007 | 0.652 | 0.496 | 0.027 | | |
| W5 | 1890 | -0.343 | 0.075 | 0.006 | 0.571 | 0.438 | 0.034 | 20.6 | 0.3 |
| W5.4 | 1930 | -0.607 | 0.066 | 0.007 | 0.639 | 0.412 | 0.046 | | |
| W5.6 | 1970 | | | | | | | | |
| W6 | 1990 | -0.536 | 0.059 | 0.008 | 0.608 | 0.407 | 0.039 | 20.1 | 0.4 |
| W6.4 | 2030 | -0.416 | 0.066 | 0.007 | 0.626 | 0.345 | 0.035 | | |
| W7 | 2090 | -0.427 | 0.069 | 0.007 | 0.664 | 0.417 | 0.025 | 28.7 | 0.3 |
| W7.4 | 2130 | -0.372 | 0.080 | 0.008 | 0.547 | 0.471 | 0.025 | | |

| | | | | | | | | | |
|---|---|---|---|---|---|---|---|---|---|
| W8.4 | 2230 | -0.525 | 0.068 | 0.007 | 0.527 | 0.370 | 0.033 | | |
| W8.8 | 2270 | -0.518 | 0.068 | 0.007 | 0.588 | 0.316 | 0.028 | | |
| W9.8 | 2370 | -0.433 | 0.059 | 0.007 | 0.553 | 0.344 | 0.034 | | |
| W10.8 | 2470 | -0.492 | 0.061 | 0.006 | 0.561 | 0.286 | 0.039 | | |
| W12 | 2590 | -0.425 | 0.080 | 0.008 | 0.576 | 0.322 | 0.016 | | |
| W13 | 2690 | -0.439 | 0.059 | 0.008 | 0.573 | 0.233 | 0.049 | | |

1017

1018

1019

| Eastbourne redox sensitive trace metal ratios performed on 0.5 M Acetic acid leachates as in reported in ref. 35. Heights from base of section. | | | | | | |
|---|---|---|---|---|---|---|
| Sample Name | Height (cm) | U/Ca (µmol/mol) | Cr/Ca (µmol/mol) | Ni/Ca (µmol/mol) | Cu/Ca (µmol/mol) | V/Ca (µmol/mol) |
| GC560 | 40 | 0.168 | 2.442 | 2.947 | 2.719 | 0.953 |
| GC500 | 100 | 0.094 | 2.412 | 1.371 | 2.840 | 0.692 |
| GC440 | 160 | 0.174 | 2.145 | 1.253 | 1.573 | 1.059 |
| GC380 | 220 | 0.118 | 2.115 | 1.372 | 2.205 | 0.766 |
| GC320 | 280 | 0.103 | 2.197 | 1.381 | 1.558 | 0.805 |
| GC260 | 340 | 0.123 | 2.784 | 2.754 | 6.432 | 0.831 |
| GC140 | 460 | 0.162 | 2.318 | 1.338 | 3.167 | 0.890 |
| GC80 | 520 | 0.129 | 2.993 | 3.446 | 5.424 | 0.841 |
| GC200 | 580 | 0.163 | 2.389 | 1.255 | 3.196 | 0.689 |
| PM40 | 640 | 0.111 | 1.556 | 4.805 | 6.998 | 0.888 |
| PM100 | 700 | 0.130 | 1.358 | 4.855 | 4.330 | 0.759 |
| PM160 | 760 | 0.088 | 1.599 | 4.339 | 4.842 | 0.814 |
| PM220 | 820 | 0.112 | 2.093 | 3.677 | 5.676 | 1.193 |
| PM280 | 880 | 0.095 | 1.399 | 4.259 | 4.122 | 0.668 |
| PM340 | 940 | 0.078 | 1.578 | 3.437 | 2.102 | 0.656 |
| PM400 | 1000 | 0.070 | 1.249 | 1.993 | 3.738 | 0.511 |
| PM440 | 1040 | 0.063 | 1.116 | 1.053 | 2.310 | 0.544 |
| PM500 | 1100 | 0.092 | 1.747 | 1.272 | 1.858 | 0.533 |
| PM540 | 1140 | 0.112 | 2.169 | 3.304 | 7.983 | 0.603 |
| PM580 | 1180 | 0.118 | 7.099 | 23.542 | 3.919 | 1.464 |
| PM620 | 1220 | 0.093 | 18.572 | 24.022 | 7.000 | 2.591 |
| PM640 | 1240 | 0.052 | 7.212 | 2.347 | 5.434 | 0.988 |
| PM680 | 1280 | 0.183 | 24.409 | 24.815 | 21.766 | 4.497 |

| | | | | | | |
|---|---|---|---|---|---|---|
| PM700 | 1300 | 0.083 | 5.164 | 1.994 | 5.227 | 1.205 |
| PM740 | 1340 | 0.086 | 11.833 | 7.012 | 18.659 | 3.679 |
| PM760 | 1360 | 0.058 | 6.489 | 2.758 | 10.789 | 2.650 |
| PM800 | 1400 | 0.083 | 1.336 | 1.692 | 2.592 | 1.283 |
| W0.4 | 1430 | 0.050 | 3.061 | 2.287 | 5.001 | 0.923 |
| WC200 | 1440 | 0.043 | 0.985 | 0.754 | 3.885 | 0.469 |
| W0.8 | 1470 | 0.057 | 1.055 | 0.869 | 5.591 | 0.764 |
| W1 | 1490 | 0.054 | 0.917 | 1.225 | 5.312 | 0.489 |
| W1.4 | 1530 | 0.037 | 0.891 | 0.864 | 3.621 | 0.266 |
| W1.6 | 1550 | 0.036 | 0.984 | 1.145 | 4.553 | 0.337 |
| W2.2 | 1610 | 0.024 | 0.859 | 0.713 | 2.871 | 0.279 |
| W2.8 | 1670 | 0.026 | 0.833 | 0.722 | 3.966 | 0.305 |
| W3.4 | 1730 | 0.030 | 0.944 | 0.982 | 4.669 | 0.376 |
| W4.2 | 1810 | 0.035 | 1.134 | 4.042 | 4.008 | 0.438 |
| W5.2 | 1910 | 0.031 | 0.883 | 0.551 | 3.502 | 0.387 |
| W5.6 | 1970 | 0.058 | 0.907 | 0.564 | 4.186 | 0.602 |
| W6.4 | 2030 | 0.030 | 0.856 | 1.914 | 7.638 | 0.419 |
| W7.2 | 2110 | 0.028 | 1.013 | 0.767 | 3.519 | 0.449 |
| W7.6 | 2150 | 0.021 | 1.285 | 0.762 | 3.872 | 0.372 |
| W8.2 | 2210 | 0.033 | 0.639 | 0.566 | 2.811 | 0.417 |
| W8.8 | 2270 | 0.028 | 0.765 | 0.575 | 2.477 | 0.318 |
| W9.4 | 2330 | 0.030 | 0.797 | 0.369 | 3.255 | 0.383 |
| W10.6 | 2450 | 0.033 | 0.698 | 0.618 | 3.270 | 0.519 |
| W11.2 | 2510 | 0.025 | 0.616 | 0.793 | 2.544 | 0.366 |
| W11.8 | 2570 | 0.030 | 1.734 | 0.936 | 4.600 | 0.423 |
| W12.4 | 2630 | 0.049 | 5.762 | 0.953 | | 1.162 |

1020

1021

1022

| Geochemical data for South Ferriby as used in Fig. 1 and S2. Heights from base of section | | | | | | | |
|---|---|---|---|---|---|---|---|
| Sample Name | Height (cm) | $\delta^{238}$Ucarb (‰) | 2SE | Mg/Ca (mol/mol) | Sr/Ca (mmol/mol) | Mn/Ca (mmol/mol) | U/Ca (µmol/mol) |
| SF-100 | 0 | -0.277 | 0.060 | 0.006 | 0.753 | 0.813 | 0.040 |
| SF-90 | 10 | -0.214 | 0.058 | 0.006 | 0.733 | 0.876 | 0.048 |
| SF-75 | 25 | -0.122 | 0.059 | 0.007 | 0.741 | 0.680 | 0.038 |
| SF-65 | 35 | -0.308 | 0.057 | 0.006 | 0.735 | 0.816 | 0.032 |
| SF-55 | 45 | -0.087 | 0.059 | 0.006 | 0.793 | 0.733 | 0.048 |
| SF-40 | 60 | -0.099 | 0.058 | 0.005 | 0.778 | 0.880 | 0.050 |
| SF-25 | 75 | -0.037 | 0.058 | 0.005 | 0.824 | 0.831 | 0.065 |
| SF-15 | 85 | -0.032 | 0.061 | 0.006 | 0.784 | 0.703 | 0.055 |
| SF25 | 125 | -0.069 | 0.060 | 0.004 | 0.661 | 0.845 | 0.070 |
| SF30 | 130 | 0.155 | 0.066 | 0.004 | 0.623 | 0.964 | 0.105 |
| SF45 | 145 | 0.544 | 0.058 | 0.004 | 0.608 | 1.016 | 0.025 |
| SF55 | 155 | -0.161 | 0.056 | 0.004 | 0.660 | 0.780 | 0.045 |
| SF60 | 160 | -0.376 | 0.045 | 0.005 | 0.633 | 0.927 | 0.024 |
| SF75 | 175 | -0.269 | 0.052 | 0.005 | 0.629 | 0.963 | 0.031 |
| SF85 | 185 | -0.342 | 0.047 | 0.004 | 0.663 | 0.801 | 0.054 |
| SF95 | 195 | -0.153 | 0.050 | 0.006 | 0.624 | 0.660 | 0.051 |
| SF150 | 250 | -0.188 | 0.064 | 0.007 | 0.505 | 0.721 | 0.020 |

1023

1024

1025

| Geochemical data for Raia del Pedale as used in Fig. 1 and S2. Heights from base of section. U/Ca presented in Fig 1 are from ref. 35 | | | | | | | |
|---|---|---|---|---|---|---|---|
| Sample Name | Height (cm) | $\delta^{238}$Ucarb (‰) | 2SE | Mg/Ca (mol/mol) | Sr/Ca (mmol/mol) | Mn/Ca (mmol/mol) | U/Ca (μmol/mol) |
| RDP0 | 0.00 | 0.280 | 0.061 | 0.021 | 0.350 | 0.000 | 2.992 |
| RDP3 | 3.00 | 0.081 | 0.067 | 0.014 | 0.207 | 0.016 | 1.710 |
| RDP8 | 8.00 | -0.522 | 0.086 | 0.769 | 0.361 | 0.112 | 8.902 |
| RDP9 | 9.00 | -0.702 | 0.070 | 0.768 | 0.300 | 0.029 | 6.639 |
| RDP16 | 16.00 | -0.872 | 0.077 | 0.720 | 0.360 | 0.035 | 11.040 |
| RDP16 | 19.00 | -0.206 | 0.076 | 0.017 | 0.256 | 0.019 | 1.272 |
| RDP22.5 | 22.50 | -0.221 | 0.092 | 0.017 | 0.250 | 0.057 | 1.323 |
| RDP32 | 32.00 | -0.126 | 0.073 | 0.018 | 0.232 | 0.032 | 0.770 |
| RDP33.25 | 33.25 | 0.175 | 0.076 | 0.016 | 0.229 | 0.021 | 0.729 |
| RDP38 | 38.00 | -0.098 | 0.070 | 0.014 | 0.179 | 0.004 | 0.548 |
| RDP39.2 | 39.25 | 0.273 | 0.067 | 0.015 | 0.191 | 0.009 | 0.407 |
| RDP42 | 42.00 | 0.607 | 0.062 | 0.011 | 0.220 | 0.020 | 0.463 |
| RDP44 | 44.00 | -0.090 | 0.069 | 0.020 | 0.292 | 0.032 | 1.176 |
| RDP51.65 | 51.65 | -0.098 | 0.070 | 0.020 | 0.281 | 0.011 | 1.688 |
| RDP56 | 56.00 | 0.819 | 0.079 | 0.016 | 0.288 | 0.006 | 0.389 |
| RDP59.25 | 59.25 | 0.175 | 0.080 | 0.020 | 0.302 | 0.048 | 0.764 |
| RDP68.25 | 68.25 | -0.093 | 0.060 | 0.019 | 0.288 | 0.015 | 1.028 |
| RDP71.75 | 71.75 | -0.112 | 0.109 | 0.012 | 0.186 | 0.013 | 0.501 |
| RDP75.5 | 75.50 | -0.130 | 0.065 | 0.021 | 0.333 | 0.006 | 0.856 |
| RDP80.5 | 80.50 | -0.089 | 0.074 | 0.014 | 0.231 | 0.019 | 0.547 |
| RDP85 | 85.00 | -0.318 | 0.085 | 0.013 | 0.195 | 0.019 | 1.067 |
| RDP89 | 89.00 | 0.019 | 0.062 | 0.014 | 0.243 | 0.042 | 0.913 |
| RDP97 | 97.00 | -0.210 | 0.087 | 0.019 | 0.252 | 0.040 | 1.001 |

1026